2

# CHAPTER 2

# Cardiovascular magnetic resonance: Basic principles, methods and techniques

*Joseph B. Selvanayagam, Matthew D. Robson, Jane M. Francis & Stefan Neubauer*

## Introduction

Unlike the physics of x-ray imaging (attenuation of x-ray beam by tissue) or the physics of ultrasound imaging (reflection of ultrasound by tissue), the physics underlying magnetic resonance imaging (MRI) is substantially more complex. This technique has evolved over the past half-century through a number of landmark discoveries and investigations. In 1946, Bloch [1] and Purcell [2] independently discovered the phenomenon of *Nuclear Magnetic Resonance*, or NMR (later shortened, although physically incorrect, to *Magnetic Resonance*, or MR), and both later shared the Nobel Price in Physics for this discovery. In 1973, Lauterbur [3] and Mansfield independently proposed that the spatial distribution of nuclear spins may be determined through local variation of field strength, i.e. by use of a magnetic field gradient; both received the 2003 Nobel prize in Medicine for this discovery. In 1976, again working independently, Radda's [4] and Jacobus's [5] groups were the first to record an MR signal from the heart, in the form of a $^{31}$P-MR spectrum. Cardiac MR spectroscopy (MRS) thus substantially preceded the development of cardiac MRI (CMR). In 1977, Damadian's group [6] reported whole-body MRI, and soon thereafter, MRI of the brain and of other non-moving or easily immobilized organs became ready for clinical prime time. The heart has long escaped high-resolution detection by MRI, because it is a constantly moving structure, posing a number of additional technical challenges to its detection by MR. CMR has come to fruition only since the mid 1990s, mainly because of major advances in hardware design (high-field, highly homogeneous magnets), coil design (cardiac phased array etc), sequence development (TrueFISP etc.) and computing power. The latter has been instrumental in speeding up image reconstruction and postprocessing, a previously critical bottleneck in CMR. In coming years, further major technical breakthroughs in CMR development are anticipated, e.g. in perfusion, coronary, and atherosclerosis imaging and in MRS. It is conceivable that, because of its unique versatility and non-invasive nature, CMR may become the primary diagnostic modality in cardiovascular medicine.

## Physical principles underlying MRI

Magnetic resonance imaging views the water and fat in the human body by observing the hydrogen nuclei in these molecules. Magnetic resonance is sensitive to any nucleus that possesses a net "spin". Nuclear spin is a fundamental property of atomic nuclei that depends on the numbers of neutrons and protons it contains, and so nuclei either have it (e.g. hydrogen ($^{1}$H), phosphorus ($^{31}$P), sodium ($^{23}$Na)) or they do not (e.g. helium ($^{4}$He), carbon ($^{12}$C), oxygen ($^{16}$O), see Table 2.1). Certain common

**Table 2.1** Myocardial tissue concentrations and MR sensitivity of elements important for MR imaging/spectroscopy.

| *Nucleus* | *Natural abundance* | *Relative MR sensitivity* | *Myocardial tissue concentrations* |
|---|---|---|---|
| $^{1}H$ | 99.98% | 100% | $H_2O$ 110 M; up to ~90 mM ($CH_3$ -$^{1}H$ of creatine) |
| $^{13}C$ | 1.1% | 1.6% | labeled compounds, several mM |
| $^{23}Na$ | 100% | 9.3% | 10 mM (intracellular); 140 mM (extracellular) |
| $^{31}P$ | 100% | 6.6% | up to ~18 mM (PCr) |

elements occur as a mixture of different isotopes, and in this case only a fraction may be visible (i.e. $^{3}He$ is visible but $^{4}He$ is not). The high concentration of hydrogen ($^{1}H$) nuclei in the human body (up to 110 mol/L) coupled with its high "relative MR sensitivity", make it the nucleus most suitable for high-resolution MRI.

Nuclei possessing net spin will behave as tiny radiofrequency receivers and transmitters when placed in a strong magnetic field. Both the frequency and the strength of the transmitter increase with increasing magnetic field strength. Typical clinical MRI systems possess fields of 1.5 Tesla (the Tesla (T) is the unit of magnetic field strength, or more accurately magnetic flux density). Even at these high magnetic field strengths the signals obtained from biological tissues are still very small, and the size of this signal can limit the quality of the images resulting in noise (graininess) obscuring the structures of interest. The nuclear magnetic resonance (NMR) phenomenon on which MRI is based involves transmitting radiofrequency pulses to the nuclei, which elevates them to a different energy level, from which they subsequently re-emit a radiofrequency signal. We can receive and acquire this re-emitted signal, and by manipulating this basic process we can perform MR imaging.

## General physics of MR

One feature of MR is that the frequency at which signals are received and re-emitted (known as the resonant frequency) is exquisitely sensitive to the exact magnetic field, for example hydrogen nuclei (lone protons) resonate at 42.575 Hz/Tesla. So, if we have two regions where the magnetic field is different by a small amount (e.g. at 1.000 Tesla and 1.001 Tesla), then the protons in one region will transmit at 42.575 MHz (the Larmor frequency for protons), and the protons from the other region will transmit at 42.575+0.042 MHz. If we sample this transmitted signal it is possible to determine these two different frequencies in the same way that a musician can distinguish between two tones at different audible frequencies. Numerically this transformation from a sampled signal to the component frequencies is known as a Fourier transform (Fig. 2.1).

Instead of using two discrete regions, in MRI we generally apply a linearly increasing magnetic field (lower at one side of the magnet and higher at the other side). As a result, each point in the body will have a discrete resonance frequency and hence the amplitude of the signal at a specific frequency will represent the number of protons at that specific location. Using a magnetic field gradient while the data are sampled allows the patient to be "imaged" in a single dimension, and comprises part of standard imaging methods. The direction of this gradient is described as the "read-out" direction in the MR image. To extend acquisition to two or more dimensions, additional switched magnetic field gradients (generally known simply as "gradients") need to be applied in the directions perpendicular to the "read-out" direction. For two-dimensional imaging, the above process is repeated a large (typically 256) number of times with different "gradients" applied in the second dimension for short intervals prior to acquisition, and the position is encoded in the phase of the signal. Each of these steps is known as a "phase encode" step and the number of these is generally[a] equal to the number of pixels in the phase-encode direction. The time

[a] This generalization is broken by partial Fourier, and by the parallel acquisition approaches (iPAT, SENSE, SMASH etc.).

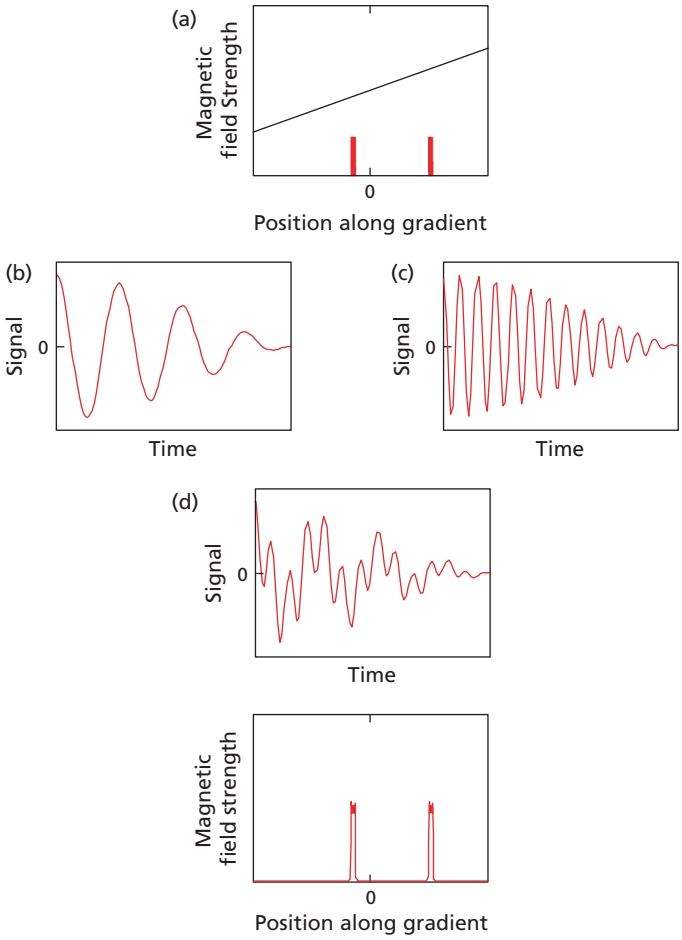


**Fig. 2.1** (a) Two regions of protons are shown within a field gradient. The signals from each of the two regions are shown ((b) and (c)), but in reality it is only the sum of these two signals that we can sample (d). By Fourier transforming the signal we can examine the sample.

required for each phase-encode step is known as the repetition time and signified as TR.

As we are interested in slices through the sample that are thin, rather than projections of the sample (as in an x-ray) we also use a process known as slice selection. This involves using a radiofrequency (RF) excitation pulse that only contains a narrow range of frequencies. By playing out such a pulse whilst a field gradient is applied we only excite nuclei within a narrow slice. By applying the above three mechanisms we can obtain a two-dimensional image from a discrete slice of the sample. By modifying the frequency of the RF pulse, and by playing out the gradient pulses on more than one axis simultaneously we can move the slice of interest freely. We are not limited to axial planes, and can acquire data with oblique or doubly oblique axes with complete flexibility.

## Basic imaging sequences

The term "pulse sequence" or "imaging sequence" describes the way in which the scanner plays out RF pulse and gradient fields and how it acquires and reconstructs the resultant data to form an image. Different orders of these pulses have defined names (e.g. FLASH, True-FISP, FSE) to describe them. The details of the sequence required for its application will also need to include the exact timings (i.e. TR), the amplitude, duration, and shapes of the gradient and RF pulses; the resolution parameters, and for cardiovascular applications these details will also include information on the cardiac gating strategy. This set of additional parameters is labeled the "protocol". Varying the protocol provides enormous flexibility for each imaging sequence.

In CMR we usually obtain 2D data acquired from a slice (e.g. 5 mm thick). Images can either be

acquired in real time or over a series of heart beats. In the first case the spatial and temporal resolution will be limited by the available imaging time. In the second case we require that the breath is held[b] and so assume that the heart is perfectly periodic and that a fraction of the phase-encoding steps of the image is acquired at the same relative phase of the cardiac cycle. The latter approach results in improved spatial and temporal resolution. If the assumption of periodicity is broken (e.g. in the case of arrhythmia, or failure to hold breath for long enough) then image artifacts[c] will result.

The basic imaging sequences used in cardiac MR are:

- FLASH (Fast Low Angle SHot). This plays out a small excitation RF pulse which is followed by a rapid read-out and then spoiling (or removing) of the residual signal to prevent it appearing as an artifact in subsequent acquisitions. The process is repeated yielding a single phase-encode line per acquisition.
- TrueFISP (aka Balanced FFE (Balanced Fast Field Echo)). This sequence is similar to FLASH but instead of spoiling the magnetization at the end of each acquisition it re-uses that signal. Compared to FLASH the benefit of this approach is that the images are of higher signal-to-noise, the disadvantages being increased sensitivity to artifacts, increased RF power deposition, and contrast that is more complex to interpret.
- FSE (Fast Spin Echo, TSE (Turbo Spin Echo)). This sequence acquires a number of phase-encode lines per acquisition by playing out a series of refocusing pulses after the initial excitation pulse. These refocusing pulses are a phenomenon of MR (not described here), which allow us to hold onto the signal created by the excitation pulse for longer so that we can sample it multiple times. The optimum excitation pulse can be used, which maximises the available signal, and it is possible with this sequence to obtain $T_2$ contrast without the undesirable effects of $T_2^*$ (see below). It is possible to acquire all the phase encodes in FSE in a single acquisition (this variant is known as HASTE, EXPRESS, and Single-Shot FSE), which has some advantages, although this is likely to result in low temporal resolution.

Additional modules can be included with the above sequences to modify the image contrast, for example:

- Black-blood pulses can be applied which effectively remove all the signal from material that moves quickly (i.e. blood). This is usually performed using double inversion, which requires a delay prior to acquisition so is most compatible with FSE-based sequences.
- Inversion recovery is a prepulse method that allows us to introduce $T_1$ contrast into an image. We can choose an inversion time that completely removes the signal from materials with a certain $T_1$. In practice this is often used when we want to see small changes in $T_1$ in late enhancement type sequences (see section on viability).
- Fat suppression (or water suppression) can be used to remove all the signal from either of these tissues, which may improve the delineation of the structures of interest.

The above acquisition approaches represent no more than the "tip of the iceberg" regarding all possible MRI acquisition strategies, but will include 95% of all practical CMR applications.

## Image contrast

If all the nuclei behaved identically, then the above imaging methods would provide a map of the patient whereby the intensity at a pixel would depend purely on the concentration of that nucleus at that location in the body. However, several additional mechanisms affect this simple picture, which make MRI a considerably more powerful technique.

- Spin-lattice relaxation ($T_1$) relates to the time it takes for the signal to recover after an excitation pulse. This can simply be thought of as the time needed for the proton system to become active again, and so if we acquire separate phase-encodes rapidly (i.e. short TR), then tissues with a long $T_1$ will not recover quickly enough and will be darkened in the image (this effect is known as

[b] Breath-holding provides the most simple and robust method for cardiac imaging. Alternative approaches do exist that involve determining the phase of breathing either using external devices, or using MRI based measurements, and dynamically modifying the scan accordingly, therefore eliminating the requirement for breath-holding. The MRI based (or navigator) methods allow for long scans where breath-holding is impossible.

[c] An artifact is an imperfection in the image that is not due purely to noise. Noise appears as a speckling of the image.

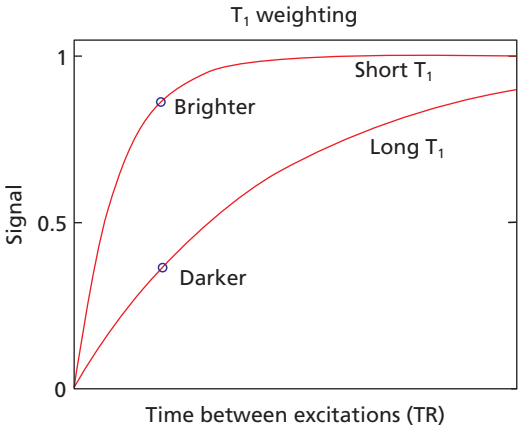


**Fig. 2.2** This oversimplified figure shows that the magnetization recovers quickly for tissues with a short $T_1$ but more slowly for tissues with a long $T_1$. By manipulating the repetition time (in this figure, but also the "flip angle") we can convert this difference in longitudinal magnetization into transverse magnetization and hence image intensity.

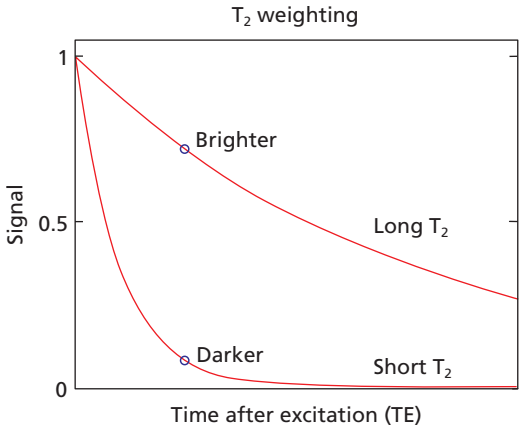


**Fig. 2.3** The transverse magnetization from the tissue with short $T_2$ decays rapidly after excitation, whereas this magnetization persists for the long $T_2$ species. These two tissues can be distinguished in an image by using a long echo time (as shown by the markers).

"saturation"), whereas tissues with a short $T_1$ will recover more quickly and so will be brighter in the image (Fig. 2.2). $T_1$ contrast can also be manipulated by changing the size of the excitation pulse (this parameter is known as the "flip angle"), as the spins will require more time to recover from the application of large flip angle than from a small one. Consequently, decreasing TR and increasing the flip angle will both increase the amount of $T_1$ weighting, whereas decreasing TR and the flip angle will decrease the amount of $T_1$ weighting.

- The spin-spin relaxation time ($T_2$) relates to the time that the signal is available for sampling after excitation. To benefit from this method we can excite the nucleus, and then wait a short period (e.g. 50 ms) before acquiring data. Tissues with a short $T_2$ (i.e. fast decay rate) will be darkened almost completely in the image, whereas tissue with a long $T_2$ (i.e. slow decay rate) will be darkened much less in the image (Fig. 2.3). $T_2$ is used to refer specifically to the relaxation rate in fast-spin-echo type sequences (i.e. the family of FSE sequences described above), and a different parameter $T_2^*$ is used to describe the equivalent time for a gradient echo type sequence (i.e. FLASH). This is useful, for example to look at iron overload where the $T_2^*$ is shortened [7]. The echo time (TE) is the time between excitation and acquisition and determines the amount that the image is affected by the $T_2^*$ and $T_2$ (known as the degree of $T_2$-weighting).
- In-flow. In the cardiovascular system the motion or flow of the protons will affect the image contrast in a similar way as the $T_1$. In this case spins may move out of the imaging slice, where they are not affected by the flip angle, to a location where they become visible in our image. In this case the in-flowing spins will have additional brightness as they will not be subject to the signal attenuation because of the effect of $T_1$ saturation (described above). MR angiography utilizes this in-flow to make blood in vessels (i.e. moving blood) bright, while suppressing the stationary signals (Fig. 2.4)

Alternative methods exist to quantitatively examine flow velocities. These methods use the field gradients to encode the position of the blood and then decode this position at a later time. Stationary signal is unaffected by this encoding and decoding, but moving tissues accumulate a change in the phase of their signal which provides quantitative information on flow rates. This method is known as "phase-velocity", as the velocity is encoded in the phase of the signal [8].

## Contrast agents

Up until this point we have only been concerned with the indigenous contrast in the sample that

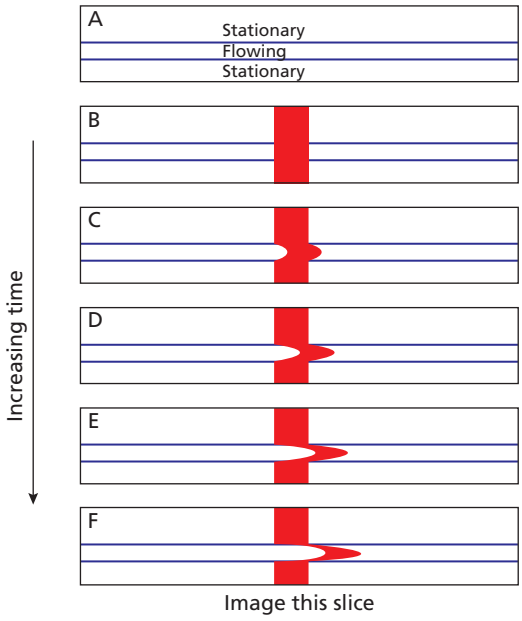


**Fig. 2.4** The above figures show the sample evolving with time. Initially (A) none of the sample is saturated. With the application of a slice selective saturation pulse a slab of signal is saturated (B). As time progresses unsaturated blood flows into the region that was previously saturated. If we select our slice thickness and imaging time correctly we can obtain an image that shows the blood without the stationary tissues.

is due to the molecular environment of the water and fat. Addition of even small amounts of certain molecules, called MR contrast agents, can massively change relaxation rates (i.e. $T_1$, $T_2$ and $T_2^*$) within the patient, which results in major changes in the appearance of an MR image. Fundamentally, there are two types of contrast agents:

- $T_1$ contrast agents, which by interaction with the nuclear spins, shorten the $T_1$ of the sample. For this to operate there needs to be intimate contact between the agent and the protons.
- $T_2$ and $T_2^*$ contrast agents. In this case the contrast agents will shorten the $T_2$ and $T_2^*$ of the sample. These effects do not need close interactions between the nuclei and the agent as they occur over much larger distances.

In each case the contrast agents are based upon molecules or ions that are magnetically active. Paramagnetic moieties (typically, Fe, Dy, Gd but also $O_2$) are used because these demonstrate the greatest effects. The most commonly used nucleus is Gd (gadolinium), and this is chelated (with diethylenetriaminepentaacetate, DTPA) so as to render it non-toxic and safe for injection. Gd compounds act predominantly as $T_1$ contrast agents in the blood and myocardium, although where the contrast cannot freely mix with the observed water (i.e. in the brain because of the blood-brain barrier), their small $T_2$ and $T_2^*$ effects can also be observed. Gd-based contrast agents are approved for clinical use, but for historic reasons at the time of writing these are not yet approved for cardiac application in the US, although this will most likely be rectified in the near future. Iron-oxide particles predominantly affect the $T_2$ and $T_2^*$ of the sample. In MR images the regions where these particles accumulate will decrease the signals in $T_2$-weighted images. For both types of contrast agent the effects are regionally specific, i.e. compounds affect the contrast at the site of the contrast agent and by an amount that increases with contrast agent concentration. This can be used, for example when looking at myocardial infarction when contrast agent remains within infarcted tissue at higher concentration than in surrounding normal tissue ~10–20 min after administration of an appropriate agent (see viability imaging). By adding MR contrast agents to compounds that can adhere to specific molecules (e.g. Fibrin) we can create "targeted contrast agents". This type of molecular imaging provides a promising approach for the future.

Contrast agents can be produced that remain within the vascular system, and are thus termed "intravascular". With an agent that decreases the $T_1$ it is possible to boost the signal in angiographic examinations, and hence improve the image quality. Presently Gd-DPTA is used in such angiographic examinations, but as it is not an "intravascular" agent the acquisition needs to occur when the Gd-DTPA is undergoing its first pass through the vascular tree. "Intravascular" contrast agents would remove this restriction, enabling longer, and hence higher quality, imaging. Presently no agents of this kind are approved for clinical use.

## The CMR scanner—how we use the physics

The physics and engineering of MRI are immensely complex, but much like a modern motor car it is not essential to understand all the details to be able to use the machine.

To minimize the effects of electrical interference from the outside world (e.g. radiotransmitters, electronic devices etc.) the MRI system is placed within an electrically shielded "box" (a Faraday cage), which is normally hidden in the walls of the scanning room. CMR scanners are a subset of MRI scanners, but with specific characteristics. Here MRI systems are described with special note as to what is required for CMR.

The most important feature of the CMR scanner is the magnet. A strong homogeneous magnetic field can be obtained by building a solenoidal electromagnet from superconducting wires carrying large electrical currents at very low temperatures. These magnets are kept permanently at magnetic field. Some clinical systems operate at 0.5, 1.0T and some new systems are available at 3.0T, but the majority of MR systems operate at 1.5T. Cardiac imaging at fields outside this range is more difficult, although scientific results have been demonstrated. The field of the magnet is highest in the centre of the bore[d] of the magnet and this is where the organs of interest (i.e. the heart and vascular system) need to be positioned. The magnetic field also extends out from the magnet. Modern systems use "active shielding" which minimizes this effect, but even with this technology the "fringe" field will extend to approximately 3–5 m (10–16 ft) or so in each direction around the magnet (including the floors above and below).

The equipment for transmitting RF pulses into the patient (the RF transmit coil), and for creating the linear magnetic field gradients (the gradient coil) are enclosed within the bore of the magnet and are not visible during operation. The gradient system on CMR machines needs to be particularly powerful because this component relates directly to the rate at which images can be acquired. The rapidly switching currents in the gradient coil interact with the magnetic field of the magnet, which results in forces being exerted on the gradient coil. The gradient coil is strongly built so as to resist these forces, but these small motions and distortions of the coil act like a speaker, producing large amounts of audible noise when running fast imaging sequences.

[d] The term "bore" is used to describe the hole through the middle of the magnet.

Additional RF reception coils are placed onto the patient, and may also be built into the patient bed, and these are used to receive the signals that are re-emitted by the nuclei. Smaller coils provide a higher signal-to-noise ratio than large coils, but also have a smaller region of sensitivity. RF coil manufacturers tailor their designs for specific parts of the body to optimise this trade off, and frequently will use multiple coils within a single structure to maximise the signal, while also maximising the region of sensitivity. These complex coil combinations are known as "phased array" coils and are standard for cardiac imaging.

The other visible component of an MRI system is the patient bed. This is required to position the patient accurately at the center of the MRI system. The MRI system is operated away from the magnet itself via a computer, which allows the operator to acquire and display images. An additional room is required to house the electronics, cooling and other control hardware associated with the MRI system; this equipment is generally hidden. Fig. 2.5 shows a typical layout of these components for a cardiovascular imaging system.

## CMR imaging techniques

### General overview of the CMR examination

Careful preparation of the patient is necessary in order to maximize diagnostic information from the CMR scan. This includes screening of the patient to exclude any contraindication to the MR examination (see section on safety), checking that the patient is not wearing any clothes with metallic fastenings, and adequate preparation of the chest prior to electrode positioning for ECG gating. To ensure good contact it may be necessary to shave the chest to remove any excess hair, and/or use an abrasive skin preparation to remove any dead skin cells and moisture. It is possible to double the amplitude of the signal with correct preparation and a simple, important rule is: "No trigger, no scan". If repeated breath-hold images are to be taken then it may be worthwhile training the patient outside the magnet about the breathing commands to be used.

Fig. 2.6 demonstrates the use of a four-lead ECG configuration and electrode positioning placed both anteriorly and posteriorly. The benefits of

**Fig. 2.5** Computer generated diagram of an MR scanning suite. The internal walls are displayed semi-opaque so each part of the system is visible. Note the operator console, magnet, and control hardware (image supplied courtesy of Siemens Medical Solutions).

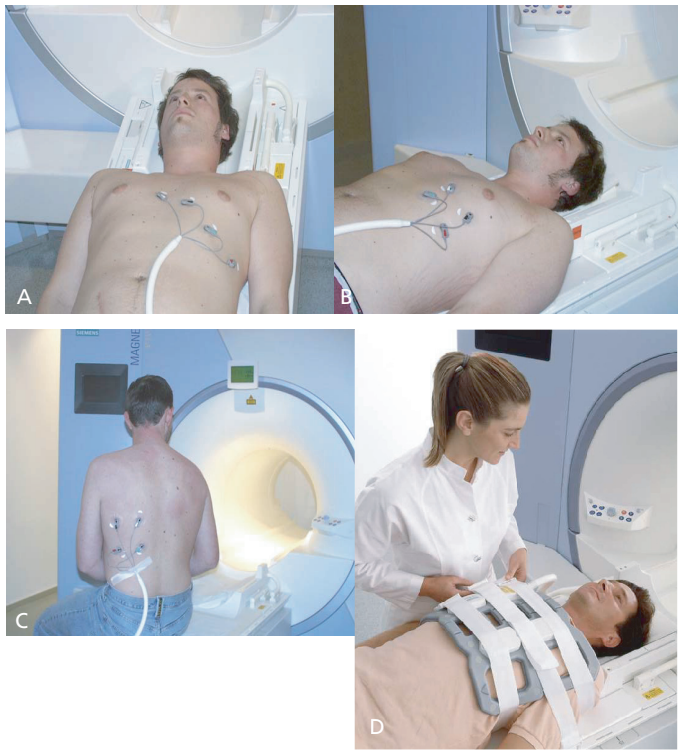


**Fig. 2.6** Suitable sites on the anterior (A, B) or posterior (C) chest wall for optimal ECG detection. (D) demonstrates the correct positioning of the body flex array coil for CMR examination. (Image supplied courtesy of Siemens Medical Solutions).

anterior lead placement are larger amplitude and ease of repositioning, but there may be respiration-induced artifacts. Posterior lead placement can help counteract this at the expense of signal amplitude. Once the patient is ready then he/she is placed supine on the scanner table and an RF receiver coil is placed over the anterior chest wall. This is used in combination with elements of the spine array coil to ensure good signal from both the anterior and posterior chest wall.

### ECG gating and physiological monitoring

Gating is described simply as the detection of the R-wave by the MR system and is used to "trigger" or synchronize the acquisition to the patient's heart rate. Correct gating relies on good R wave detection

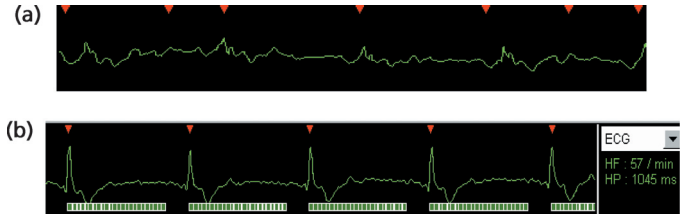


**Fig. 2.7** (a) An example of poor R wave recognition in a patient positioned within the magnet bore. In contrast (b), there is accurate R wave detection during this prospectively gated cine acquisition. Cine frames are indicated by the green squares below the trace.

and a regular R-R interval. Deterrents to successful CMR imaging include poor R wave detection (Fig. 2.7), an inadequate ECG, and the presence of tachyarrhythmias and/or ventricular ectopic beats. When using prospective cardiac gating, the MR system detects the R-wave and then begins the imaging sequence. However, as this method only uses 80–90% of the R-R interval, data are not acquired during end-diastole.

Retrospectively gated sequences are now widely available, whereby the sequence is continuously repeated, the R-R interval monitored and the data retrospectively fitted, allowing acquisition of the entire cardiac cycle. This method has the added benefit of compensating for some variation in the R-R interval during acquisition. A new feature of some CMR systems is arrhythmia detection, which allows the R-R interval that is used for acquisition to be fixed by the operator, thus eliminating data obtained during ectopic beats. This approach may particularly aid data acquisition in patients with atrial fibrillation.

One important consideration is the effect of the magnetic field on the ECG waveform. Blood flow, particularly in the aorta, causes an additional electrical signal detected by the ECG, leading to a magnetohydrodynamic effect. This is generally superimposed on the T wave and can make the analysis of the ECG within the magnetic field very difficult. The only diagnostic feature of the ECG that is reliable while a patient is inside the bore is the heart rate (provided QRS detection is good), whereas it is difficult to comment on changes in the P wave, the ST segment and the T wave. The development of techniques such as the vector ECG, which uses 3D collection of ECG data and separates artifact from the true ECG signal, have helped to overcome some of the ECG problems associated with CMR and to improve image quality and scan efficiency [9]. Another novel method of ECG synchronization is the self gating approach where information regarding cardiac motion is extracted from the image data [10]. This method does not require an ECG to be obtained.

The other main cause of image degradation in CMR is respiration-artifact. Most patients are able to hold their breath during image acquisition, particularly with the recent introduction of parallel imaging techniques such as iPAT and SENSE which reduce breath-hold times considerably. However, especially in instances where the patients cannot hold their breath (e.g. older subjects, significant cardiac/respiratory disease), and/or in cases where longer acquisition times are unavoidable (e.g. coronary artery imaging), respiratory gating with MR navigators is essential for artifact free images. Navigator echo techniques are used for respiratory compensation, in conjunction with ECG gating. The navigator echo is combined with the imaging sequence and enables movement to be tracked throughout the respiratory cycle. It consists of a signal from a column perpendicular to the direction of movement. The usual placement for CMR is on the dome of the diaphragm, and the sequence only acquires when the diaphragm is in a predefined position with a small tolerance window. Although this might reduce scan efficiency and hence prolong imaging time, it does allow acquisition to take place with the patient breathing freely (Fig. 2.8). Fig. 2.9 shows some common artifacts encountered during CMR imaging.

## Cardiac anatomy

Cardiac anatomy can easily be demonstrated using MR imaging techniques, which are not confined to the three orthogonal planes (transverse, coronal and sagittal) as in conventional imaging. The multiplanar capabilities of CMR can be used to define the conventional imaging planes of the heart, such as the horizontal and vertical long axes, and the

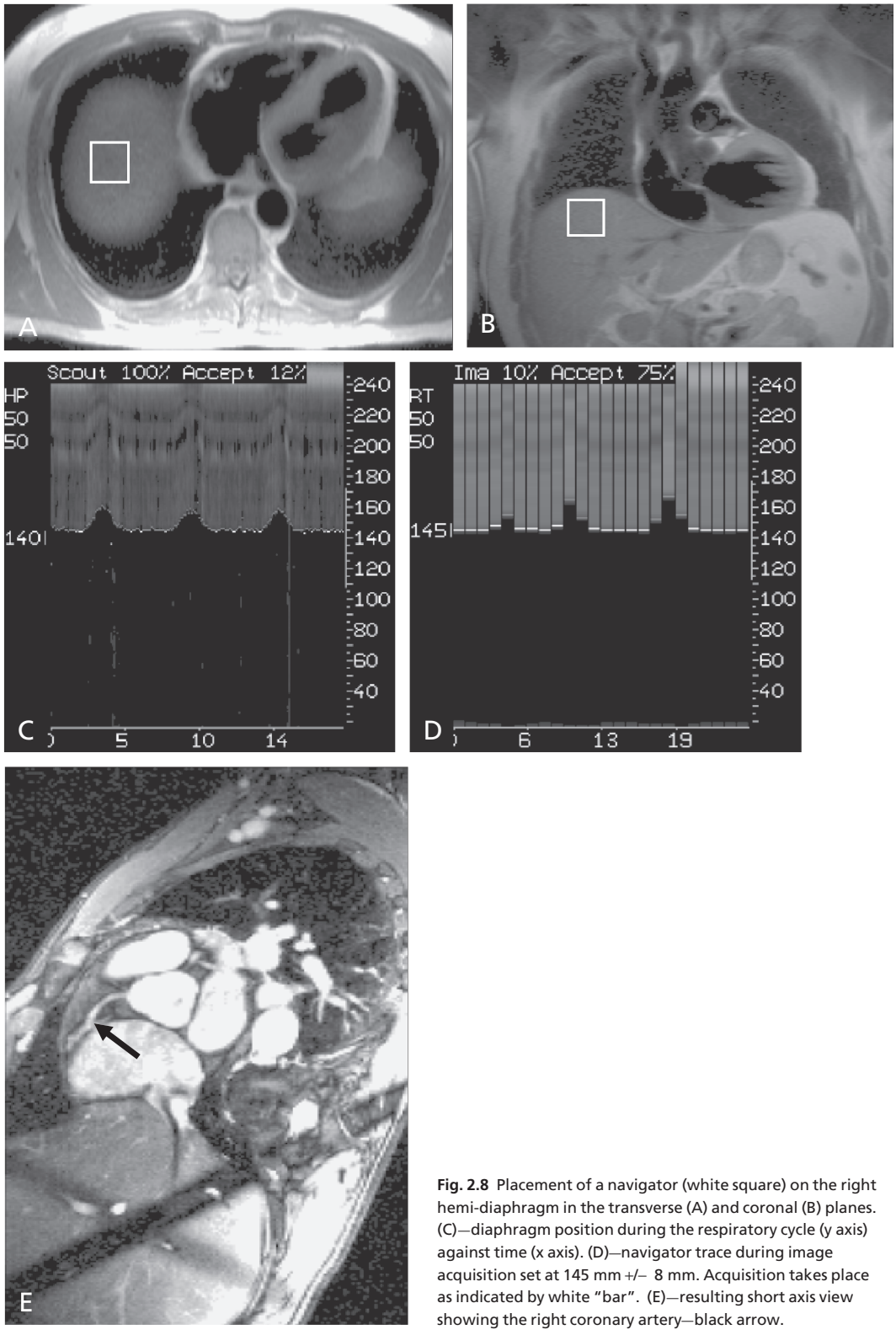


**Fig. 2.8** Placement of a navigator (white square) on the right hemi-diaphragm in the transverse (A) and coronal (B) planes. (C)—diaphragm position during the respiratory cycle (y axis) against time (x axis). (D)—navigator trace during image acquisition set at 145 mm +/– 8 mm. Acquisition takes place as indicated by white "bar". (E)—resulting short axis view showing the right coronary artery—black arrow.

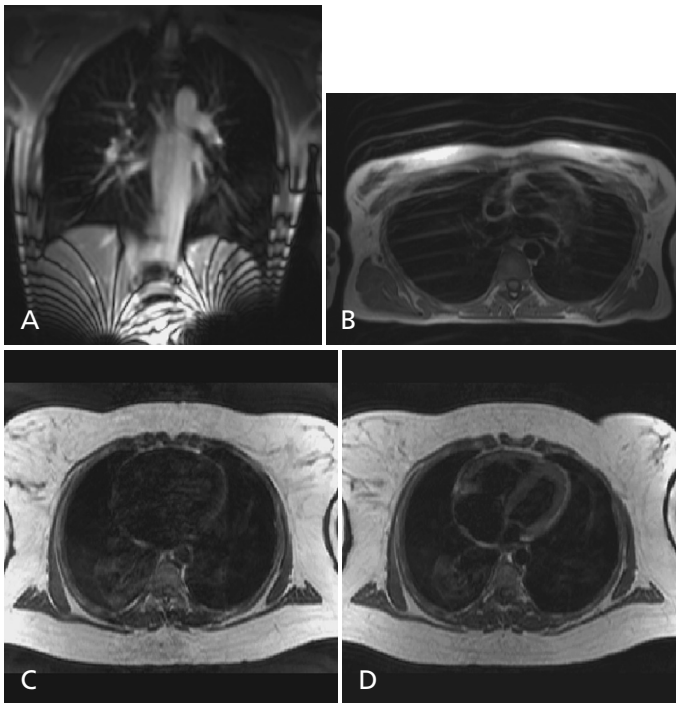


**Fig. 2.9** Common artifacts seen during CMR imaging: (A) Metal artifact from a small clip in the patient's trousers, highlighting the importance of removing all clothing with metal fastenings. (B) Respiration artifact during a spin echo anatomical imaging sequence. (C) Poor definition of cardiac structures with spin echo sequence because of incorrect positioning of ECG electrodes. (D) Significant improvement seen after repositioning of the ECG electrodes.

short axis, as well as to prescribe any imaging plane specific to a particular pathology. This is particularly useful in cases of congenital heart disease. The three orthogonal planes (see Fig. 2.10) remain important for diagnosis and these can be easily and quickly acquired using the newer single shot techniques such as HASTE, where a stack of images can be obtained in a single breath-hold.

The transverse plane is useful for a good overview of size, shape and position of the cardiac chambers and great vessels and should be inclusive from the top of the aortic arch (including the great vessels) to the inferior wall of the right ventricle, typically covering 20–24 slices. The coronal plane is useful for an assessment of the descending aorta, IVC (inferior vena cava) SVC (superior vena cava), both ventricles, left atrium and pulmonary veins, and the LVOT (left ventricular outflow tract). The slices should reach from the descending aorta posteriorly to the right ventricle anteriorly. The sagittal plane is useful for visualizing the descending aorta, IVC (inferior vena cava), SVC (superior vena cava), and the right ventricle. In addition, the oblique sagittal view, which is planned from the transverse multislice series can be a useful addition when assessing the aorta and gives the familiar "hockey stick" view of the whole of the aorta.

## Cardiac function

CMR has rapidly become the imaging method of choice and the gold standard in the assessment of cardiac function of both normal and abnormal ventricles [11–14]. Given its 3D nature and order of magnitude greater signal-to-noise ratio, CMR is highly superior to 2D echocardiography for the measurement of global left ventricular function [11]. This has allowed reductions of study sizes of 80–97% to achieve the same statistical power

**Fig. 2.10** (*opposite*) Anatomical images obtained with a turbo spin echo sequence showing the heart and great vessels in a transverse (A-D), coronal (E-H) and sagittal (I-K) planes. (L) shows an oblique sagittal view of the ascending and descending aorta, the so called "hockey stick" view. LV denotes left ventricle; RV denotes right ventricle; MPA, main pulmonary artery; RVOT, right ventricular outflow tract; AA, proximal ascending aorta; DA, descending aorta; LA, left atrium; RA, right atrium; SVC, superior vena cava; PDA, proximal descending aorta.

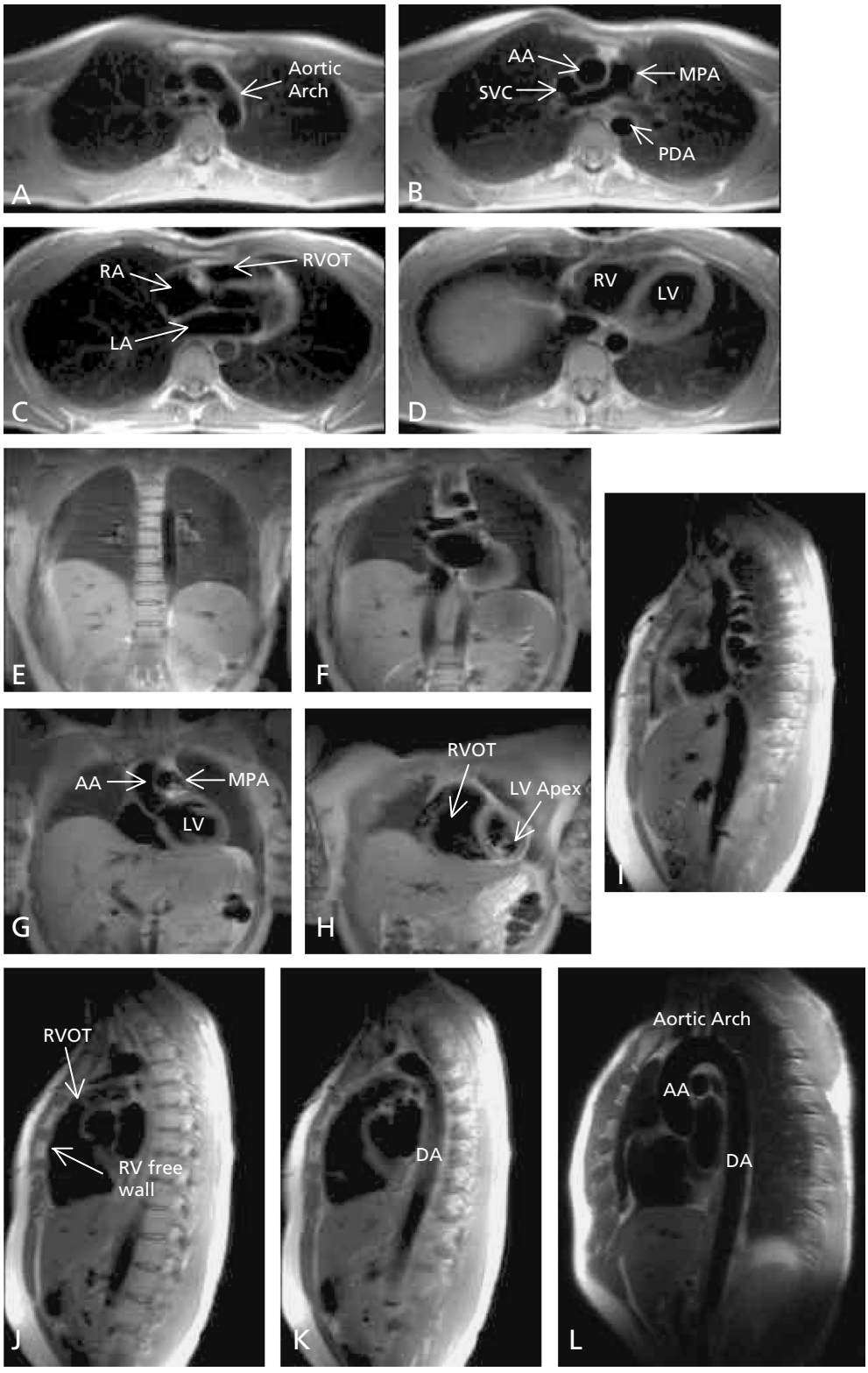

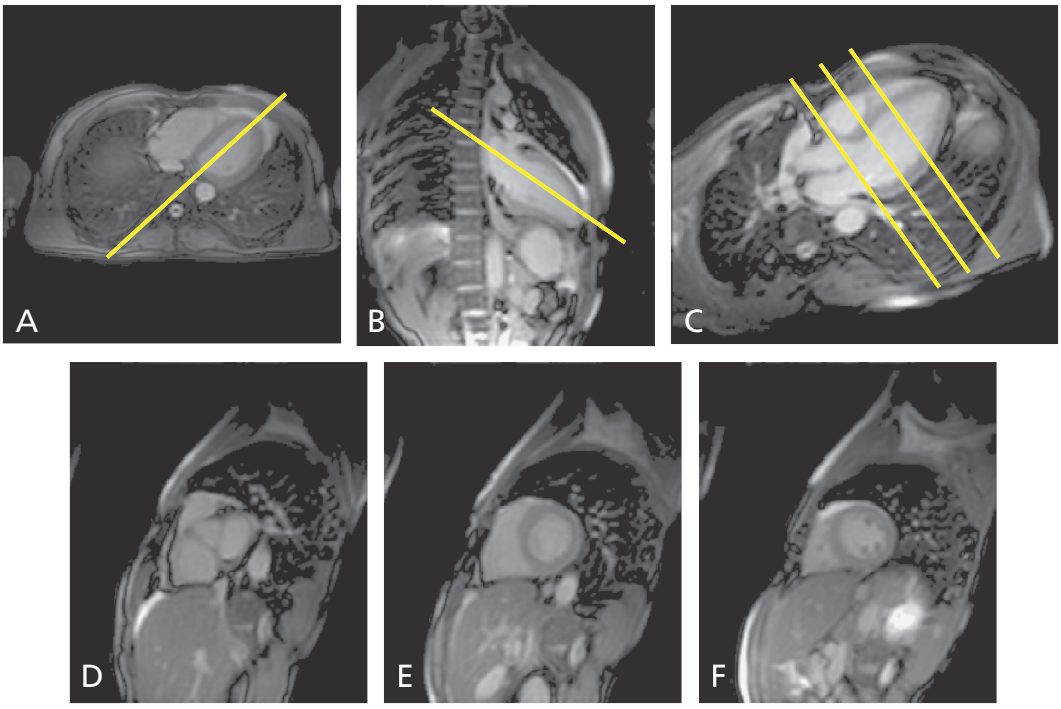


**Fig. 2.11** Sequence of images (A-F) demonstrating the correct acquisition of the long axis and short axis planes for cine imaging. Initially, multiplanar localizer images are performed in a single breath-hold (A). Using the transverse localizer (A), in the plane indicated by the solid line in (A), pilot images are then performed in the vertical long axis (VLA) plane (B). The resultant VLA pilot is used to prescribe (as indicated by the solid line in (B)) the horizontal long axis (HLA) pilot (C). Using the HLA and VLA pilots, three short axis (SA) slices (D-F) are next acquired with the basal slice parallel to the atrioventricular (AV) groove (indicated by three solid lines in (C)).

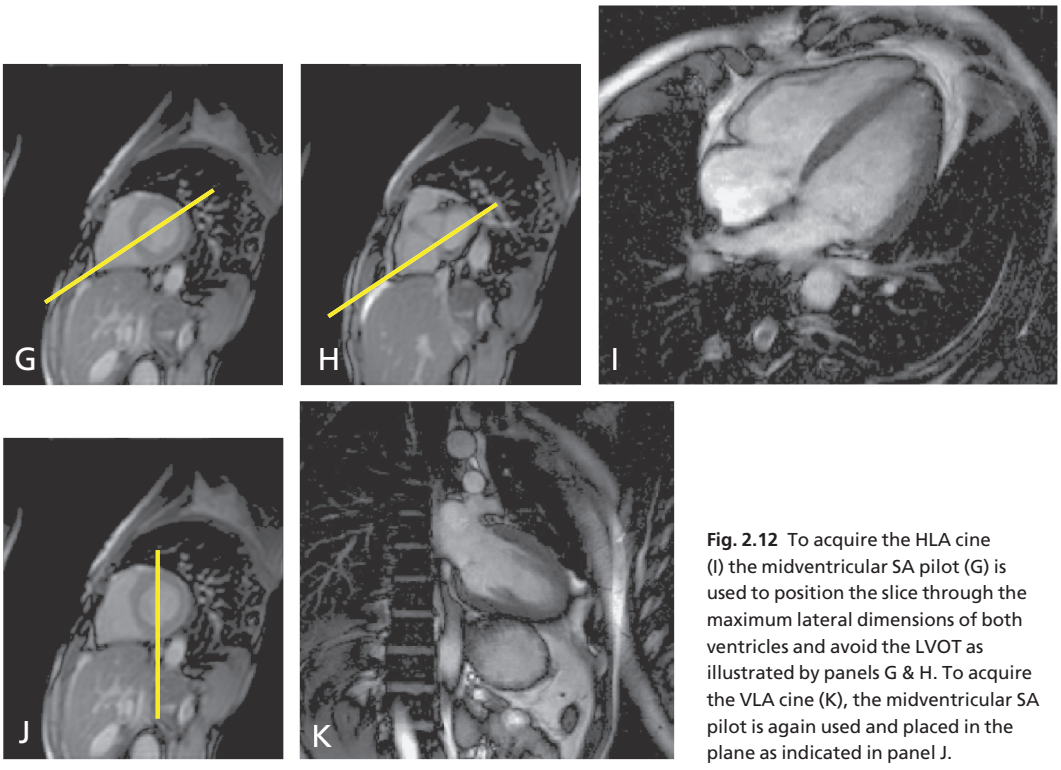


**Fig. 2.12** To acquire the HLA cine (I) the midventricular SA pilot (G) is used to position the slice through the maximum lateral dimensions of both ventricles and avoid the LVOT as illustrated by panels G & H. To acquire the VLA cine (K), the midventricular SA pilot is again used and placed in the plane as indicated in panel J.

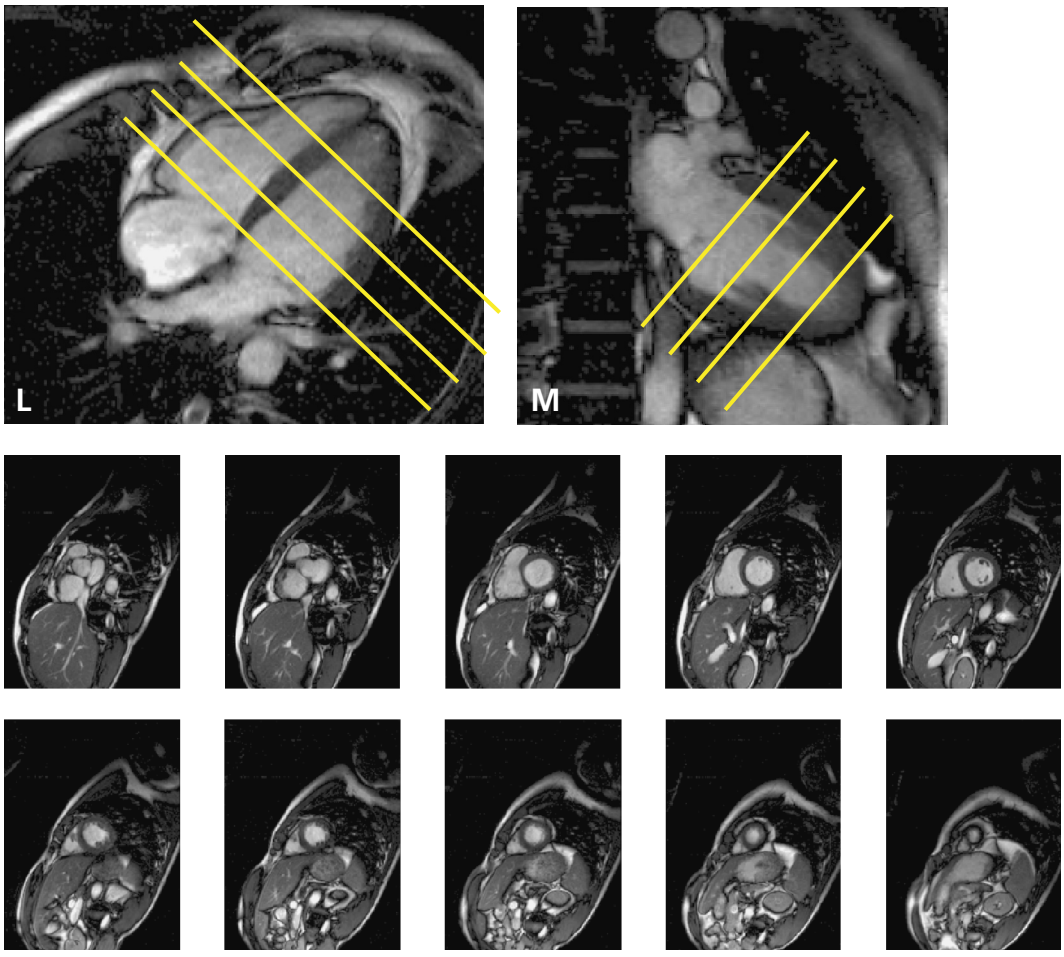


**Fig. 2.13** This demonstrates the resultant HLA (L), VLA (M) and short axis cine stack from base to apex (bottom panel). Placement of only 4 short axis slices shown for image clarity.

for demonstrating given changes of left ventricular volumes, ejection fraction, or cardiac mass [11]. It can be performed quickly and easily, and can be incorporated into a comprehensive CMR examination.

The following method is employed at the authors' institution, and is a widely accepted approach to quantify left ventricular volumes, mass and function (Fig. 2.11, Fig. 2.12 and Fig. 2.13). The methods described may not be possible from all manufacturers, and variations from the described protocol may be necessary. After careful preparation of the patient and explanation of the importance of consistent breath-hold technique, multislice, multiplanar localizer images are performed in a single breath-hold. Prescribing a plane from the transverse plane using the mitral valve and the apex of the left ventricle as anatomical markers, localizer ("pilot") images are obtained in the vertical long axis (VLA). The resultant VLA pilot is then used to prescribe the horizontal long axis (HLA) pilot using the same anatomical landmarks.

It is important to accurately define the base of the heart when using this or a similar piloting method. As illustrated in Fig. 2.11, using the HLA and VLA pilots, three short axis (SA) slices are acquired with the basal slice parallel to the atrioventricular (AV) groove. The distance between the slices is chosen such that they encompass the basal, mid and apical regions of the left ventricle. These "scout" images can then be used to plan cine images in two long-axis (HLA, VLA), and left ventricular outflow tract (LVOT) views.

When acquiring the short axis volume stack

from the two long axis cines, the position of the basal slice is critical. Most errors in volume calculation are introduced here if this stage is not carefully planned. Using the end-diastolic frames from the VLA and HLA cines, the first slice is placed in the atrioventricular (AV) groove. Subsequent slices are placed parallel to this, covering the entire left ventricle. Typically slice thickness is 7–8 mm with a 3 or 2 mm interslice gap. Imaging is usually performed in expiration as this generally produces a more consistent, reproducible breath-hold position.

Volume and mass data are calculated by drawing epicardial and endocardial regions of interest (ROI) at end-systole and end-diastole. Papillary muscles and trabeculae should be included in mass calculation and excluded from ventricular volumes. Various programmes are available to aid calculation of these values, e.g. ARGUS ® (Siemens Medical Solutions), and MASS ®, (Medis, Netherlands). Normal, gender specific values for left and right ventricular volumes and mass in adults have been defined [14]. Earlier studies used a gradient echo approach, such as a turboFLASH sequence, which has inferior blood/myocardial contrast definition when compared to newer steady state acquisition techniques such as TrueFISP. Recent studies have provided normal volume and mass ranges using steady state free precession (SSFP) sequences [13]. These show that SSFP sequences produce larger ventricular volumes and smaller ventricular mass measurements (when compared to gradient echo sequences) in the same reference population due to the improved definition of the blood-endocardial border.

CMR is also considered to be the most accurate imaging method for the evaluation of right ventricular (RV) volumes. CMR measurement of RV volumes has been validated with close correlation between RV and LV stroke volumes, and between RV stroke volumes and tricuspid flow measurements [15]. The inherent 3D nature of CMR makes it particularly well suited to studying the RV, given its complex and variable (even in normal volunteers) morphology [16]. CMR measurements of the RV volumes can either be acquired in a transverse (axial) orientation or in an axis aligned along the LV short axis. Both methods have their advantages and limitations. Using the LV short axis plane, only one data set is required for both LV and RV measurements. In addition, in the images acquired using the axial orientation, the partial volume effect of blood and myocardium on the inferior wall of the RV can make it difficult to identify the blood/myocardial boundary. However, assessment of the RV in the LV short axis orientation also has important limitations: The position of the pulmonary and tricuspid valves cannot be clearly identified and therefore, the basal boundary of the RV can be difficult to define. This can result in significant error because the basal slice has a large area. In a recent study that compared the two methods for RV volume measurements, Alfakih *et al.* found that there were systematic differences between them, and that the axial orientation resulted in better inter and intra-observer reproducibility [17].

### Dynamic measures of left ventricular function

Given its ability to visualize myocardial segments accurately, CMR can be used to define ventricular function during pharmacological stress, principally with dobutamine (DSMR). Although DSMR imaging has been performed since 1992 [18], early studies to document inducible myocardial ischemia were limited by an inability to image the entire cardiac cycle during peak stress, and concerns about patient safety. Recent software and hardware advances have enabled the investigators to overcome some of these limitations. Shorter repetition times, phase encoding grouping and phased array surface coils allow for acquisition of images with high temporal resolution and with spatial resolution sufficient to delineate the endocardial border during peak stress [19]. Earlier concerns about patient safety have been alleviated by the introduction of hemodynamic monitoring and wall motion display software that allows the physician to safely monitor patients during stress testing.

### Practical Aspects of DSMR Imaging

In preparation for a DSMR study patients are instructed to refrain from taking any ß-blockers and nitrates 24 hours prior to the examination. Short acting ß-blocker (e.g. Esmolol 0.5 mg/kg) is used as an antidote and should be easily accessible during scanning. Table 2.2 details the monitoring requirements needed for stress MR imaging. As with its use in other cardiac imaging, severe arterial hypertension (>220/120 mmHg); recent acute coronary syndrome; significant aortic stenosis; complex cardiac arrhythmias, and significant hypertrophic obstructive cardiomyopathy are some of the contraindications to the use of dobutamine stress testing.

**Table 2.2** Monitoring requirements needed for stress MR imaging.

| | |
|---|---|
| Heart rate and rhythm | Continuously |
| Blood pressure | Every minute |
| Pulse oximetry | Continuously |
| Symptoms | Continuously |
| Wall motion abnormalities | Every dose increment |

*Scan protocol:* All 17 segments of the heart can be covered by a combination of three SA and two long axis views (HLA, VLA). The three SA and two long axis cines are performed at rest and are also repeated during stress at each dobutamine dose. Scans are terminated when the submaximal heart rate is reached; systolic blood pressure decreases >20 mmHg below baseline; blood pressure increases >240/120 mmHg; intractable symptoms, and new or worsening wall motion abnormalities occur in at least two adjacent left ventricular segments, or in the presence of complex cardiac arrhythmias.

*Image interpretation:* Multiple cine loop display is recommended, showing at least four different stress levels for each slice simultaneously. The ventricle is analyzed by 17 segments per stress level [20]. Analysis is carried out visually according to the standards suggested by the American Society of Echocardiography. Segmental wall motion is classified as normokinetic, hypokinetic, akinetic or dyskinetic and assigned one to four points, respectively. The sum of points is divided by the number of analyzed segments and yields the wall motion score. Normal contraction results in a wall motion score of one, a higher score is indicative of wall motion abnormalities. During dobutamine stress with increasing doses, a lack of increase in either wall motion or systolic wall thickening, a reduction of both, or significant changes in the rotational pattern of left ventricular myocardium ("tethering") are indicative of pathological findings. Nagel *et al.* compared DSMR imaging to dobutamine stress echocardiography (DSE) in patients referred for diagnostic coronary angiography [21]. They showed that DSMR imaging provided superior specificity (86% vs 70%) and sensitivity (89% vs 74%) in detecting coronary stenosis >50%, principally because the number of myocardial segments visualized as "good" or "very good" image quality was far greater with DSMR than with DSE. Among patients with regional wall motion defects at rest, DSMR has been shown to have a sensitivity of 89% and specificity of 85% for identifying coronary artery stenosis greater than 50% [22].

### Tissue contractility

Beyond analysis of global and segmental function, MR offers techniques for assessment of regional and tissue contractility.

*MR tagging:* This method was first developed by Zerhouni and colleagues [23]. A radiofrequency tag is a region within the imaged tissue where the net magnetization has been altered with radiofrequency pulses. Each tag or "saturation grid" is created as a 3D plane that extends through the tissue, and it is seen as a tag line when imaged in an orthogonal view (Fig. 2.14). Typical tagging schemes include stacks of parallel lines [24], grids [25], and radial stripes [26]. By tracking material points as a function of

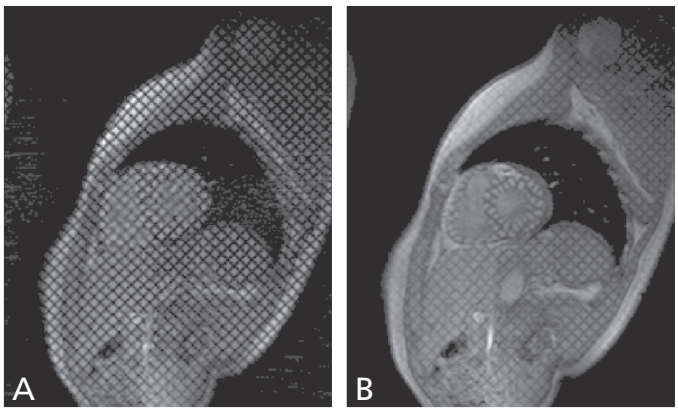


**Fig. 2.14** Cardiac tagging short axis images obtained in a normal heart using a complementary spatial modulation of magnetization (CSPAMM) technique. The initial rectangular tagging grid at diastole (A) is distorted by cardiac contraction, as seen in the end-systolic image (B).

time, it is possible to compute the description of motion around a given point in the tissue as it traverses through time and space. Although the concept of radiofrequency tagging was proposed over a decade ago, automated software to analyze the images has only recently become available, [27, 28] and the clinical use of the method remains to be determined.

*Tissue phase mapping and DENSE:* The tissue phase mapping technique allows the determination of three-dimensional velocity tensors over the cardiac cycle, i.e. for rotation, radial and longitudinal movement, with a pixel-by-pixel spatial resolution nearing that of "conventional" cine MRI [29]. This is currently being investigated in clinical studies. Displacement encoded imaging using stimulated echoes (DENSE) can also provide information on myocardial displacement, velocity and strain [30].

## Assessment of myocardial viability

Viability assessment can be defined practically as detecting myocardium that shows severe dysfunction at rest, but which will improve function, either spontaneously with time (stunned) or following revascularization (hibernating). The identification of residual myocardial viability is critical to the management of patients with ischemic heart disease. Contrast-enhanced MRI (ceMRI) with gadolinium-DTPA was described in 1984 in a canine model of acute MI [31]. Injured myocardium demonstrates significantly greater T1 shortening after contrast. These initial studies were hampered, however, by insufficient image contrast between normal and injured myocardium due to technical (e.g. gradients, phased array etc.) and sequence limitations.

### Delayed enhancement MRI

In recent years, a number of studies have demonstrated the effectiveness of a segmented inversion recovery fast gradient echo (seg IR-GE) sequence for differentiating irreversible injured from normal myocardium with signal intensity differences of nearly 500% [32]. This technique of delayed enhancement imaging (DE-MRI), pioneered by Simonetti, Kim and Judd, has been shown in animal and human studies, to identify the presence, location, and extent of acute and chronic myocardial irreversible injury [33–36]. Delayed enhancement MRI (DE-MRI), allows assessment of the transmural extent of irreversible injury, and is superior to SPECT for the identification of subendocardial myocardial infarction [37–39]. Furthermore, it permits quantification of even small areas of myocardial necrosis, both due to native coronary disease and, after percutaneous and surgical revascularization [40–42].

### Practical aspects of delayed enhancement image acquisition

Delayed enhancement imaging can be performed in a single brief examination, requiring only a peripheral intravenous line. It does not require pharmacological or physiological stress. Initially cine images are obtained (as described above) to provide a matched assessment of left ventricular morphology and contractile function. A bolus of 0.10–0.20 mmol/kg intravenous gadolinium is then given by hand injection. After a 10–15 min delay (see below), high spatial resolution delayed-enhancement images of the heart are obtained at the same imaging planes as the cine images using the segmented IR-FGE pulse sequence. Each delayed-enhancement image is acquired during a 10–14 s breath-hold, and the imaging time for the entire examination (including cine imaging) is generally 30–40 min. Fig. 2.15 demonstrates two patient examples.

### Segmented inversion recovery fast gradient echo sequence (IR-GE)

The timing diagram for the segmented IR-GE pulse sequence is shown in Fig. 2.16. Immediately after the onset of the R wave trigger, there is a delay period before a non-selective 180° inversion pulse is applied. Following this inversion pulse, a second variable wait period (usually referred to as the inversion time or TI), occurs corresponding to the time between the inversion pulse and the centre of acquisition of k-space lines. The flip angle used for radiofrequency excitation for each k-space line is shallow (20°–30°) to retain regional differences in magnetization that result from the inversion pulse and TI delay.

The following factors need to be considered when performing DE-MRI:

*Dose:* The dose of gadolinium given is usually 0.1–0.2 mmol/kg. Early validation studies used doses as high as 0.3 mmol/kg in animal models [34] and

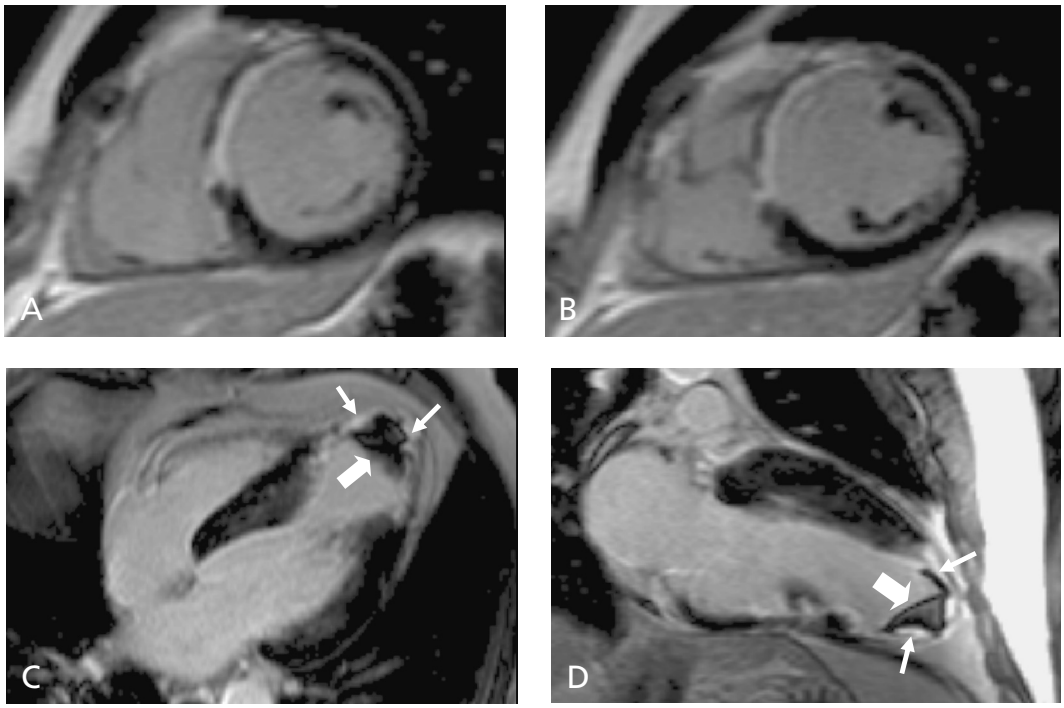


**Fig. 2.15** Two patient examples of delayed hyperenhancement (DHE) imaged with a segmented inversion recovery gradient echo sequence at 10 min postGd-DTPA injection (0.1 mmol/kg). Panels A–B, demonstrate anteroseptal DHE in a patient presenting with two-week-old anterior myocardial infarction and proximal left anterior descending artery (LAD) occlusion. C–D are from a patient with history of apical myocardial infarction 12 months prior and midLAD occlusion, showing thinned apical wall with fully transmural DHE (small arrows). Co-existent apical thrombus is also seen in this patient (large arrows).

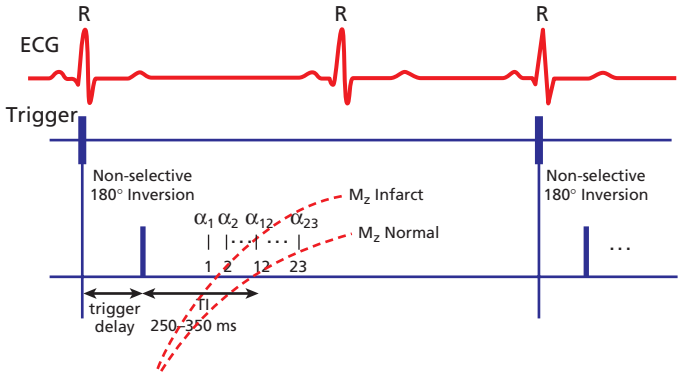


**Fig. 2.16** Timing diagram of two-dimensional segmented inversion-recovery fast gradient echo pulse sequence. ECG = electrocardiogram, TI = inversion time delay, $\alpha$ = shallow flip angle excitation. See text for further details. (Figure re-drawn from: Reference 32, Simonetti OP, Kim RJ, Fieno DS *et al*. An improved MR imaging technique for the visualization of myocardial infarction. *Radiology* 2001; **218**: 215–223. Re-drawn with permission of publishers.)

0.2 mmol/kg in patients [43]. More recent studies have found that using 0.1–0.15 mmol/kg still provides excellent image contrast between injured and normal myocardium with the added advantage that the time required to wait after contrast administration is reduced [41, 44]. It is necessary to allow the blood pool signal in the LV cavity to decline and provide discernment between LV cavity and hyperenhanced myocardium. This is particularly important in imaging small subendocardial infarcts, and when using a higher dose (i.e. 0.2 mmol/kg).

*Gating factor:* Image contrast is also optimized by applying the inversion pulse every other heart beat in order to allow for adequate longitudinal relaxation between successive 180° inversion pulses. If there are limitations related to breath-hold duration and/or bradycardia, every heart beat imaging may have to be performed. In this situation there may be incomplete relaxation of normal myocardium. Incomplete relaxation will result in not only an artificially shorter "effective" TI needed to null normal myocardium, but may also lead to a reduction in the image intensity differences between infarcted and normal myocardium.

*Inversion time (TI):* This is defined as the time between the 180° pulse and the center of acquisition of the k-space lines. Selecting the appropriate TI is probably the most important element in obtaining accurate imaging results. The TI is chosen to "null" normal myocardium, the time at which the magnetization of normal myocardium reaches the zero crossing (Fig. 2.16). This is when the image intensity difference between infarcted and normal myocardium is maximized. If the TI is too short, normal myocardium will be below the zero crossing and will have a negative magnetization vector at the time of k-space data acquisition. Since the image intensity corresponds to the magnitude of the magnetization vector, the image intensity of normal myocardium will increase as the TI becomes shorter and shorter, whereas the image intensity of infarcted myocardium will decrease until it reaches its own zero crossing.

At the other extreme, if the TI is set too long, the magnetization of normal myocardium will be above zero and will appear gray. Although areas of infarction will have high image intensity, the relative contrast between infarcted and normal myocardium will be reduced. Usually only one or two "test" images need to be acquired as with experience one can estimate the optimal TI based on the amount of contrast agent that is administered and the time after contrast agent administration. As the gadolinium concentration within normal myocardium gradually washes out with time the TI will need to be adjusted upwards (e.g. 10 ms every 3–4 images) to provide optimal image quality with multiple time-point imaging. Recently available automated TI finding sequences can also help in establishing the optimal inversion time.

### Postprocessing

For routine clinical reporting, the 17-segment model recommended by the American Heart Association can be used [20]. The extent of hyperenhanced tissue within each segment is graded visually using a 5-point scale in which a score of 0 indicates no hyperenhancement; 1, hyperenhancement of 1–25% of the segment; 2, hyperenhancement of 26–50% of the segment; 3, hyperenhancement of 51–75% of the segment, and 4, hyperenhancement of 76–100% of the segment. It is advisable to interpret the delayed-enhancement images with the cine images immediately adjacent which provide a reference for the diastolic wall thickness of each region.

## Assessment of myocardial perfusion

Contrast agents based on paramagnetism (e.g. gadolinium) or superparamagnetism (e.g. $Fe^{2+}$) can be tracked as they traverse the myocardium after intravenous injection to assess myocardial perfusion at rest and with a vasodilator (e.g. adenosine). Quantitative results have been achieved in animal studies with an intravascular agent such as a macromolecular blood pool marker, although such compounds are not yet licensed for use in humans. At the same time, semiquantitative/quantitative approaches are feasible in humans with a conventional extracellular MR contrast agent (Gd-DTPA).

### First pass imaging

In first pass imaging a bolus of contrast agent is injected directly into a peripheral vein and a sequence of images is then obtained to show the dynamic passage of the tracer through the heart (Fig. 2.17).

### MR sequences and contrast agents

The most significant parameter that a perfusion sequence must optimize is the temporal resolution, because the contrast agent only spends a relatively short period of time passing through the myocardium. During this time the required data must be obtained at a sufficient rate so that the reconstructed images provide a measure of the change in contrast agent concentration over time. For a complete perfusion study, up to three to five separate short axis slices need to be simultaneously obtained to achieve sufficient coverage of the myocardium. The most commonly used perfusion sequences are turboFLASH, SSFP, multishot echo planar (EPI)

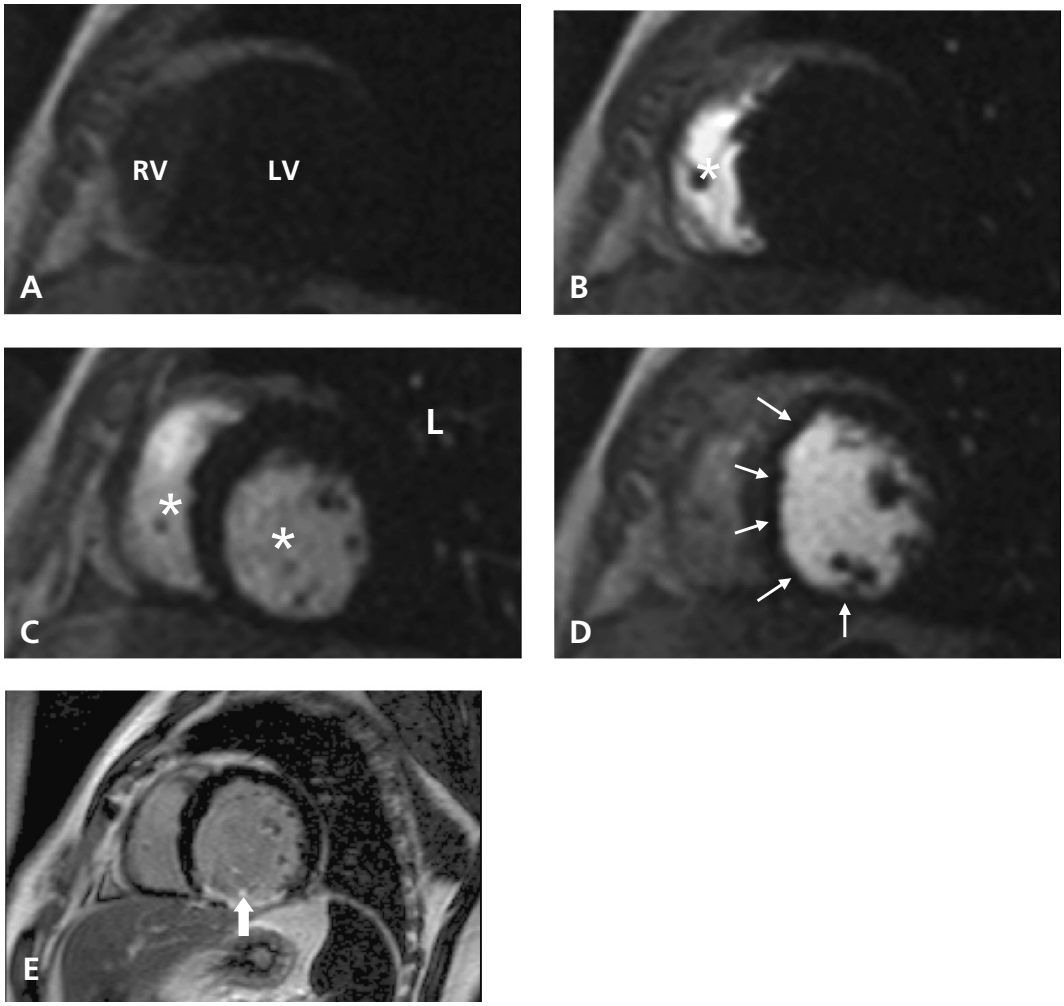


**Fig. 2.17** Example of CMR perfusion images obtained with a turboFLASH sequence during first pass rapid injection of an extracellular contrast agent (Gd-DTPA). Images were acquired in a basal short axis view, and show: (A)—before contrast injection, (B)—contrast agent first in the right ventricle, (C)—contrast agent then in the lungs and left ventricle and (D)—agent in the left ventricle cavity and myocardium. Perfusion defect is seen in the anteroseptum, inferoseptum and inferior wall (arrows). Corresponding "delayed enhancement" image (E) is shown at the same slice position, demonstrating inferior wall delayed hyperenhancement (block arrow). Patient had evidence of significant left anterior descending artery and right coronary artery disease. RV = right ventricle, LV = left ventricle, L = lungs, * = contrast agent.

and hybrid EPI-gradient echo (GRE) sequences. Fast $T_1$ weighted imaging sequences such as spoiled gradient-echo imaging with TRs as short as 2 ms and a magnetization preparation (either inversion recovery or saturation recovery) for $T_1$ weighting are applied to image the contrast enhancement during the first pass of contrast agent.

The most common compound bolus used is an extracellular MR contrast agent such as Gd-DTPA. Rapid contrast injection is crucial as this improves the sensitivity for detecting changes in myocardial perfusion [45]. The goal is to assure that the primary bottleneck to the rate of contrast enhancement is the rate of transport of the contrast through the myocardial tissue and not the rate at which the contrast agent is injected. The regional image intensity contrast enhancement should ideally be proportional to the contrast agent concentration.

Such an approximate linear relationship between regional signal intensity and contrast agent concentration is only observed at lower contrast agent dosages—typically, <0.05 mol/Kg of Gd-DTPA for fast IR-prepared gradient echo sequences (TR < 3 ms; TE < 2 ms) [46].

**Vasodilator stress**

A complete discussion of the effects of adenosine/dipyridamole is beyond the scope of this chapter. Briefly, vasodilation with dipyridamole or adenosine induces an increase of blood flow in myocardial areas supplied by normal coronary arteries ("coronary steal"), whereas no (or only minimal) change is found in areas supplied by stenotic coronary arteries. With adenosine a maximal coronary vasodilation can be achieved safely with an intravenous infusion at a rate of 140 μg/kg/min. For cardiac imaging 4–6 min of infusion is recommended. The vasodilatory effect of adenosine may result in a mild to moderate reduction in systolic, diastolic and mean arterial blood pressure (<10 mmHg) with a reflex increase in heart rate. Although some patients may complain about anginal chest pain or dyspnea, these effects respond promptly to discontinuation of the drug and usually do not require medical intervention. Studies in over 10,000 patients during thallium radionuclide imaging, echocardiography, SPECT and MRI have shown that pharmacological stress testing with adenosine presents a safe method of acquiring stress imaging data [47, 48]. However, adenosine should be used with caution in patients with pre-existing atrioventricular (AV) block or bundle branch block and should be avoided in patients with high-grade AV block, sinus node dysfunction or reversible airways obstruction (e.g. asthma).

**Practical aspects of image acquisition**

An intravenous line should be started before the examination for administration of the contrast agent. A16G or 18G peripheral needle is usually sufficient together with a power injector at a rate of 5–10 ml/s. Contrast administration needs to be followed without delay by an injection of physiologic saline solution to assure that the entire contrast agent dose is injected into the vein. Monitoring of the patient's blood pressure, heart rate, and, preferably, also the arterial oxygen saturation is recommended.

Practical tips that aid successful perfusion imaging:
**1** The recommended contrast agent dose varies from 0.02 mmol/kg to 0.1 mmol/kg Gd-DTPA depending on the sequence used and the type of assessment needed (quantitative versus qualitative).
**2** Double oblique slices that give a short axis view of the heart are recommended. For multislice acquisitions the interslice gap should be 30–50% of the chosen slice thickness. Slice positions are customarily chosen to cover the location of wall motion defects that are detected on the cine imaging, which is usually performed beforehand.
**3** Minimize the field of view without causing aliasing ("wrap around") artifacts. It is our practice to perform a test image (without contrast) to determine any wrap artifact and to adjust the slice position accordingly. Choosing the read-out direction parallel to the chest wall often reduces the likelihood of aliasing and other artifacts.
**4** Perform the scan with the patient holding their breath in inspiration. Begin the scan as soon as the patient starts the breath-hold; the contrast agent injection can be started after acquisition of three to five "baseline" images.

**Qualitative analysis and visualization**

Currently, only limited data is available regarding the accuracy of visual assessment, and experience is required to reach an acceptable standard. The main artifacts occurring during the initial passage of the contrast bolus are due to susceptibility at the endocardium blood-pool interface, sometimes making diagnosis of subendocardial perfusion deficits difficult. The trabeculae of the papillary muscles are especially prone to susceptibility artifacts and such findings should not be interpreted as evidence of a regional ischemic perfusion abnormality.

**Semiquantitative analysis**

Most publications in the literature have been based on semiquantitative analysis of regional myocardial perfusion. Here the endo- and epicardial contours of left ventricular myocardium are traced and corrected manually for changes of diaphragmatic position due to breathing or diaphragmatic drift. The myocardium is then divided into six to eight equiangular segments per slice, and an additional region of interest is placed within the cavity of the left ventricle, excluding the myocardial segments

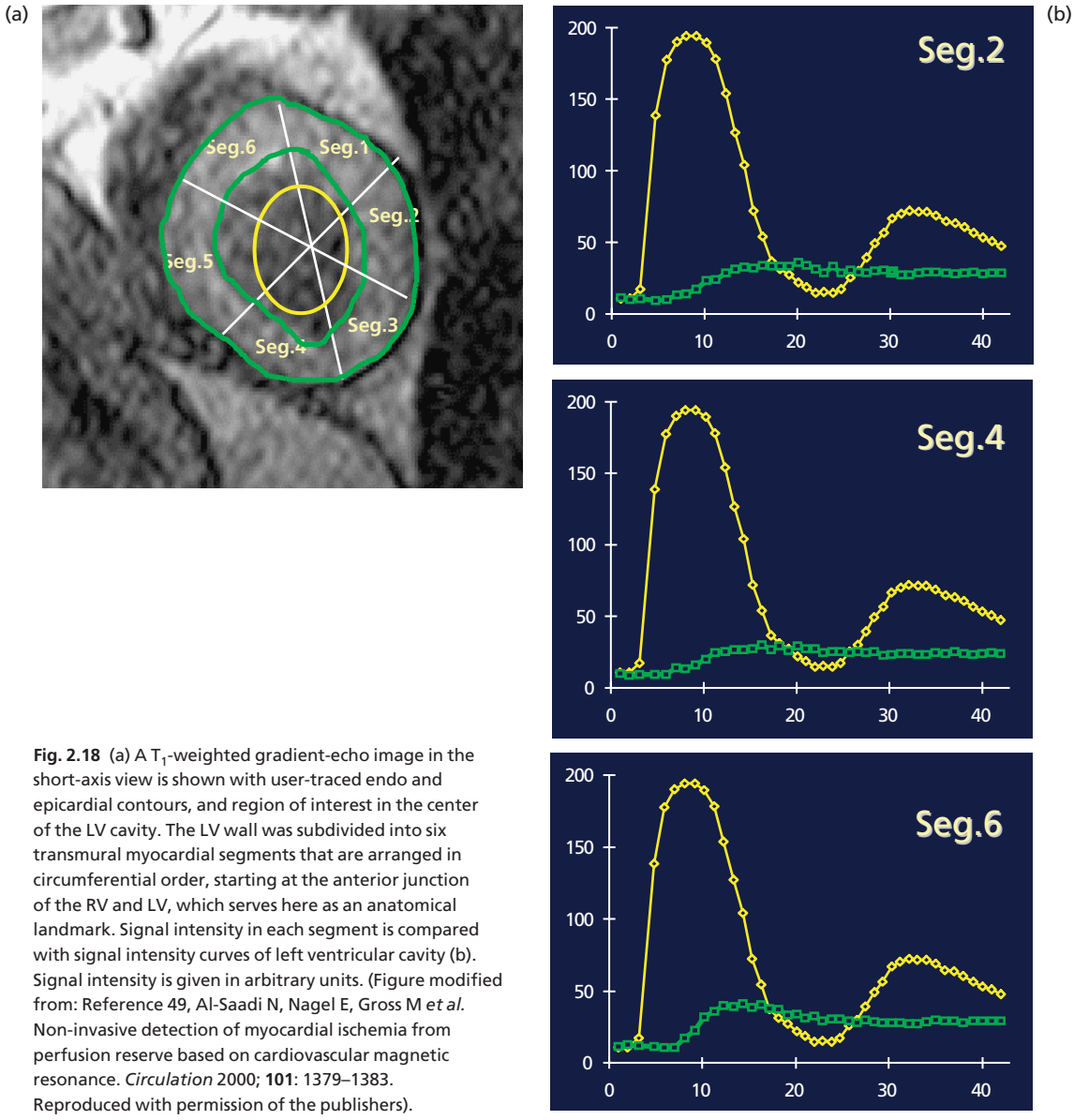


**Fig. 2.18** (a) A $T_1$-weighted gradient-echo image in the short-axis view is shown with user-traced endo and epicardial contours, and region of interest in the center of the LV cavity. The LV wall was subdivided into six transmural myocardial segments that are arranged in circumferential order, starting at the anterior junction of the RV and LV, which serves here as an anatomical landmark. Signal intensity in each segment is compared with signal intensity curves of left ventricular cavity (b). Signal intensity is given in arbitrary units. (Figure modified from: Reference 49, Al-Saadi N, Nagel E, Gross M *et al.* Non-invasive detection of myocardial ischemia from perfusion reserve based on cardiovascular magnetic resonance. *Circulation* 2000; **101**: 1379–1383. Reproduced with permission of the publishers).

and the papillary muscles (Fig. 2.18 and Fig. 2.19). Images acquired after premature ventricular beats or insufficient cardiac triggering need to be excluded from the analysis to guarantee steady-state conditions. Signal intensity is determined for all dynamics and segments. The upslope of the resulting signal intensity time curve is determined by the use of a linear fit. To correct for possible differences of the input function, the results of the myocardial segments are corrected by dividing the upslope of each myocardial segment by the upslope of the left ventricular signal intensity curve. Perfusion reserve index is calculated by dividing the results of stress imaging by the results obtained at rest.

### Quantitative analysis

Quantification of myocardial blood flow and measurement of myocardial perfusion reserve is based both on the Fermi model of constrained deconvolution, as well as on other independent models

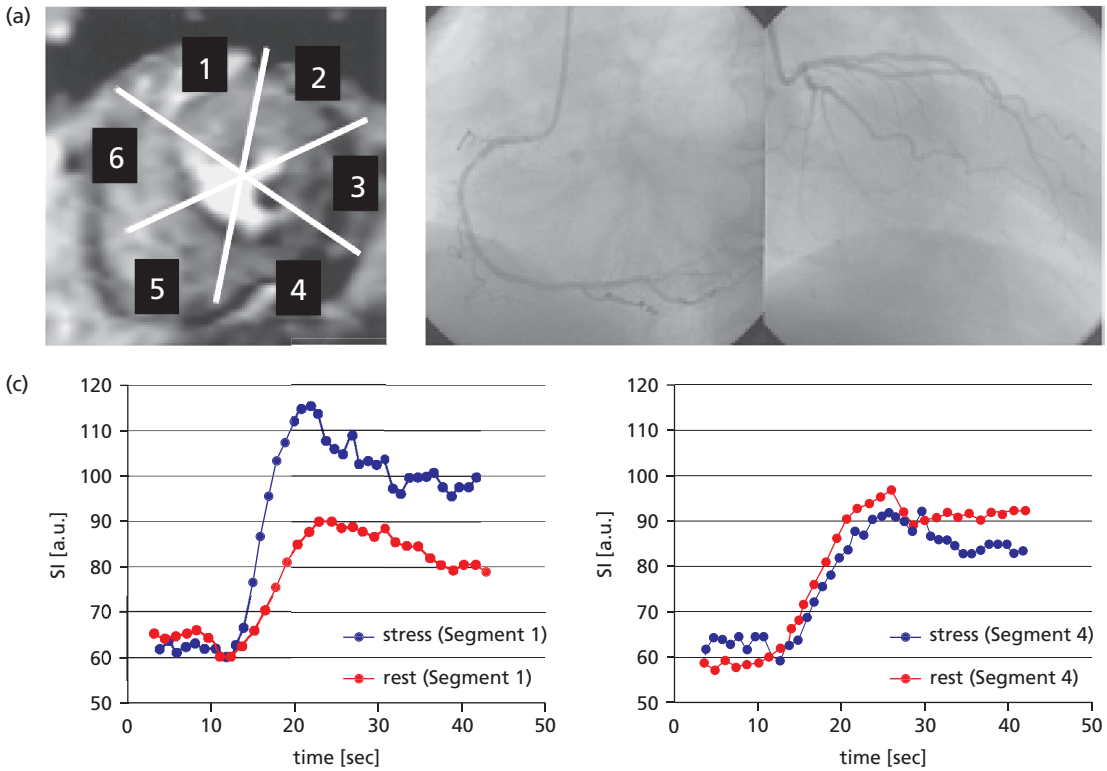


**Fig. 2.19** (a) Segmentation of the myocardium into six equiangular segments per slice, starting clockwise from the anterior septal insertion point of the right ventricle. (b) Coronary angiogram of the patient showing critical right coronary artery stenosis. In the normally perfused anterior segment, there is a clear increase of the upslope after adenosine (●) when compared with rest (●), whereas in the inferior segment of the same slice there is no change of the upslope after vasodilation (c). (Figure re-drawn from: Reference 47, Nagel E, Klein C, Paetsch I *et al*. Magnetic resonance perfusion measurements for the non-invasive detection of coronary artery disease. *Circulation* 2003; **108**: 432–437. Re-drawn with permission of the publishers.)

[50–52]. Compared to the Fermi-model-based analysis, model-independent deconvolution provides an impulse response that is a more accurate representation of the true impulse response, albeit at the price of higher complexity in the implementation of the algorithms. The model-independent analysis works well for analyzing contrast enhancement with intravascular and extracellular contrast agents. For the extracellular contrast agents, the Fermi model requires that the fit to the measured data be limited to approximately the first pass, as the leakage of contrast agent from the vascular space into the interstitial space is not reproduced well by the Fermi impulse response model. The model-independent analysis overcomes this shortcoming of the Fermi model [53]. However, more experience, as well as standardization of the analysis method will be needed to determine the clinical value of absolute quantification of perfusion.

*Future requirements:* A general limitation to MR perfusion imaging using gadolinium contrast is the use of different technical approaches by different vendors and different centers, which discourages comparison of results and limits multicenter trials. A standardized approach is needed both for image acquisition (e.g. image sequences, contrast dose, number of slices etc) as well as postprocessing (e.g. color coded maps). This would then pave the way for long term, multicenter trials in larger heterogeneous patient groups, which are necessary to establish the prognostic value of this technique in coronary artery disease.

### Non-contrast perfusion and BOLD Sequences

Spin labeling techniques exploit the labeling of the nuclear magnetization of water protons, either by direct preparation of inflowing spins or by specific preparation of the imaging slice. In both cases, water

is used as a free diffusible contrast agent. Although easily repeatable, arterial spin labeling techniques applied at 1.5 Tesla yield only a relatively small signal difference between normal and underperfused myocardium (44% in a recent study by Wacker *et al.* [54]), but these techniques may become more practical when applied at higher field.

Blood oxygenation level-dependent (BOLD) MRI may overcome the tracer kinetic limitations of first pass perfusion imaging by observing changes in tissue oxygenation directly. BOLD utilizes the $T_2^*$ effect, that is the incoherence in the phase behavior due to local inhomogenities in the magnetic field. Wacker and colleagues show that dipyridamole was associated with an increase of $T_2^*$ in healthy volunteers but with a $T_2^*$ decrease in patients with stenotic coronary arteries [55]. Although significant progress is being made [54, 56], BOLD imaging is not yet ready for clinical application to the heart as it is currently only possible to analyze single slices and the $T_2^*$ signal differences remain small. The arrival of 3T systems hold much promise in this regard, as at 3 Tesla the blood $T_2$ is much more sensitive to its oxygenation level than it is at 1.5 Tesla, consequently intravascular contrast (a significant mechanism for BOLD in the myocardium) will be increased at 3 Tesla.

## Measurement of blood flow

Velocity encoded cine (VENC) MR imaging allows accurate estimation of velocity profiles across a valve or any vascular structure, comparable to those provided by Doppler ultrasonography [57, 58]. In addition, MR imaging is able to quantify flow volumes and does not have the same limitations with respect to acoustic penetration of different portions of the heart and therefore is better able to demonstrate distribution and velocity of flow throughout the heart. On cine gradient-echo MR images, blood has bright signal intensity due to fresh inflowing blood that has not been saturated. Abnormal flow patterns encountered in valvular disease cause dephasing of the spins within a voxel and result in signal loss (flow void). This flow void is seen with either stenosis or regurgitation and is caused by high-velocity flow and turbulence [59]. Its appearance depends on technical factors including display parameters (window width and level), flip angle and TE [60]. With long-TE sequences (12 ms), the flow void is well demonstrated, whereas with short-TE sequences (<7 ms), it tends to be smaller. These variables must be taken into account when evaluating flow anomalies.

Flow-sensitive imaging techniques permit the measurement of flow expressed as either velocity or volume per unit of time. Currently, the most popular flow-sensitive cine MR imaging technique is referred to as phase-contrast, phase-shift, or velocity encoded (VENC) MR imaging. As described in the section on image contrast, this is based on the principle that the phase of flowing spins relative to stationary spins along a magnetic field gradient changes in direct proportion to flow velocity. Magnitude images can be reconstructed to provide anatomical information, and phase images can provide flow velocity information. The phase shift is displayed as variations in pixel signal intensity on the phase map image. Stationary tissue appears gray on this image, whereas flow in a positive direction along the flow-encoding axis will appear bright, and flow in a negative direction will appear dark (Fig. 2.20). As a result, it is possible to differentiate antegrade from retrograde flow. Furthermore, as with Doppler ultrasonography, the phase map image can be color coded to reinforce the differentiation between antegrade and retrograde flow. Velocity can be encoded in planes that are perpendicular to the direction of flow by using section-selective direction (through-plane velocity measurement), in planes that are parallel to the direction of flow by using phase encoded or frequency encoded directions (in-plane velocity measurement), or, more recently, in 3D. However, VENC MR imaging also has certain limitations and potential sources of error [61]. Because of the cyclic nature of phase, aliasing may appear if more than one cycle of phase shift occurs. To avoid aliasing, which occurs when the chosen velocity range is lower than the predicted maximum velocity, the velocity threshold must be correctly selected prior to acquisition.

VENC MR imaging can be used to calculate absolute velocity at any given time during the cardiac cycle at specified locations in the plane of data acquisition. Velocity can be measured for each pixel within a region of interest encircling all or part of the cross-sectional vessel area or across a valve annulus. The product of cross-sectional area (as determined from the magnitude image) and spatial

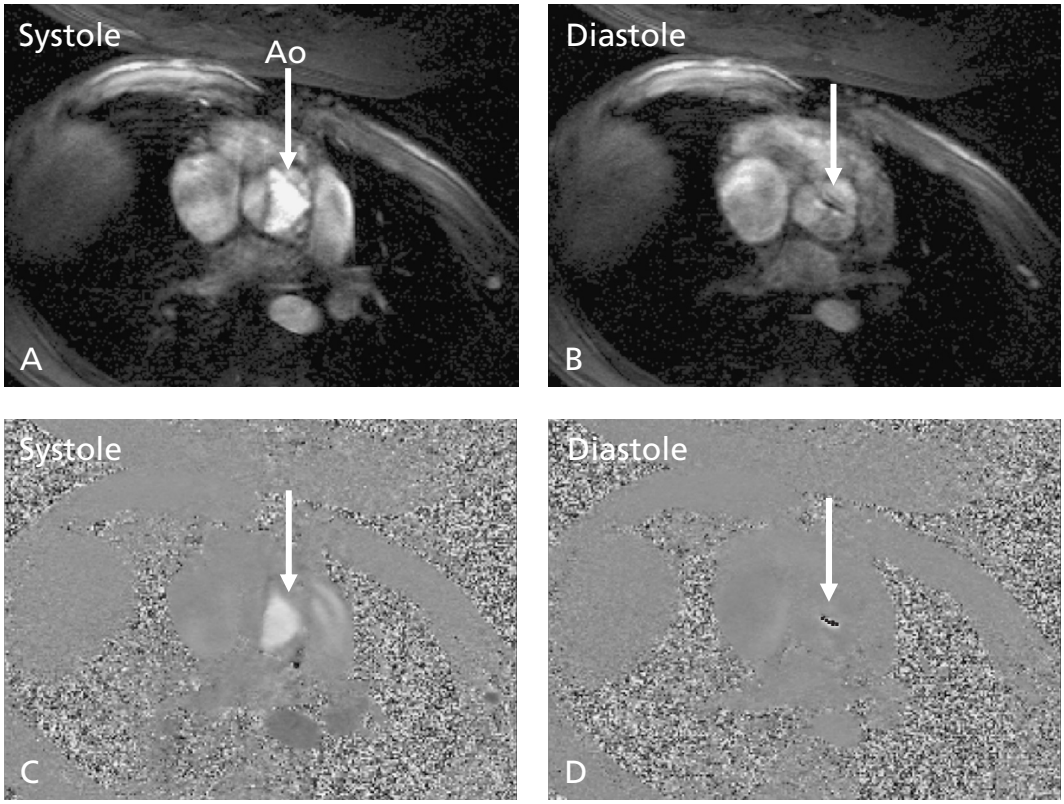


**Fig. 2.20** Transverse velocity encoded MR magnitude (A, B) and phase (C, D) images centered on the aortic valve in a patient with severe aortic regurgitation. In systole (A, C), the leaflets are open and bright signal, indicating anterograde flow (arrows). In diastole (B, D) absence of coaptation is demonstrated, and dark signal indicates central retrograde flow. In (D), there is also adjoining lighter area due to aliasing effects.

mean velocity (i.e. the average velocity for all pixels in the cross-sectional area on the phase image) yields the instantaneous flow volume for each time frame during the cardiac cycle. Integration of all instantaneous flow volumes throughout the cardiac cycle yields the flow volume per heart beat. This technique has been evaluated *in vitro* as well as *in vivo* by several authors and allows accurate measurement of aortic and pulmonary arterial flow, which represent the stroke volumes of the left and right ventricles, respectively [62]. It has also been used to calculate the ratio of pulmonary to systemic flow, thereby allowing non-invasive quantification of left-to-right shunts [63] and separate measurement of right and left pulmonary flows [64]. Moreover, these measurements can be used in the evaluation and quantitative assessment of valvular regurgitation and stenosis.

## MR angiographic techniques

In recent years there has been considerable interest in magnetic resonance angiography (MRA) in which images of blood vessels are produced without detail from surrounding stationary tissue. MRA techniques fall into three broad categories: Time of flight (TOF), phase contrast and contrast-enhanced MRA. These have applications in imaging various vessels, particularly the aorta, carotid, renal, and peripheral arteries.

*Time of flight MRA (TOF MRA):* Time of Flight MRA relies on the flow of fully relaxed material into the imaged volume for image contrast (see earlier section on image contrast). Fast gradient echo imaging is commonly used to perform 2D or 3D TOF MRA. In the former, thin slices are acquired one at a time, while in the latter, a volume is excited by the radiofrequency (RF) pulse.

*Phase contrast MRA:* Phase contrast MRA relies on changes in the phase of the transverse magnetization induced by the application of a bipolar, flow sensitized gradient, which generate a phase difference between the stationary tissues and the moving blood. Phase contrast angiography has effective background suppression and provides quantitative flow measurements, but the acquisition time is long and the technique is only sensitive to a certain range of blood velocities.

*Contrast-enhanced MRA (CE-MRA):* This has become an increasingly popular angiographic technique over recent years as it can be acquired during a single breath-hold, and hence has particular advantages in imaging areas of major respiratory motion such as the thorax and abdomen. The appropriate intravenous injection of Gd-DTPA leads to substantial local blood signal enhancement because of the shortening of the $T_1$ relaxation time of blood. Timing of the scan with respect to the intravenous bolus is critical for data collection. Consequently, it is good practice to administer a "test bolus" to estimate the contrast arrival time at the targeted vessel. Contrast-enhanced MRA is the preferred MRA technique for the evaluation of aortic aneurysms, pulmonary arterial disease, and peripheral arterial disease. Renal CE-MRA is indicated in patients with hypertension to exclude vascular causes, and in patients with worsening renal function to exclude bilateral renal artery stenosis.

**Coronary and bypass graft imaging**

The epicardial coronary arteries are small structures, demanding images of high spatial resolution. For such high resolution imaging the need for high signal-to-noise (SNR) and contrast-to-noise (CNR) ratios often means prolonged imaging time. However, longer imaging time makes the image vulnerable to motion-related blurring, artifact and image degradation. Hence, adequate cardiac and respiratory motion suppression (see earlier section) is imperative for artifact free coronary imaging.

The principal sequences used for coronary imaging (summarized below) utilize the "time of flight" angiography principle that was mentioned above. "Black blood" coronary MRA (CMRA) takes advantage of the negative contrast between flowing coronary blood and surrounding tissues. "Black blood" methods may be particularly useful for patients with bypass grafts or intracoronary stents, as they are less sensitive to metallic implant susceptibility artifacts than gradient echo ("bright blood") imaging. Contrast-to-noise ratio can also be improved by the use of MR contrast agents. Gadolinium-based agents considerably reduce the $T_1$ relaxation time of blood, resulting in an improved differentiation between coronary blood and the adjoining myocardium. Imaging can be done using saturation recovery or inversion recovery prepulses. Extracellular agents appear best suited to first pass breath-hold approaches, whereas intravascular contrast agents may be best for longer navigator/free breathing CMRA.

Proximal coronary artery visualization has been the main aim of CMRA since initial studies were performed more than 10 years ago [65, 66]. This showed that visualization is possible of proximal segments in a majority of motivated volunteers and patients. Two of the most commonly used techniques for CMRA, which are performed at various CMR centres, are briefly described below (Fig. 2.21). A full discussion of all the available techniques is beyond the scope of this chapter, but is available elsewhere [68].

*3D segmented k-space gradient echo CMRA:* First described by Li [65] and Botnar [69], this technique takes advantage of superior SNR and postprocessing capabilities of 3D imaging and provides high spatial resolution. As the data acquisition period is long, exceeding standard breath-hold duration, navigators are needed for respiratory gating. The use of $T_2$ preparatory pulses are also needed to enhance CNR and facilitate better identification of the coronary arteries from underlying tissue.

*3D segmented k-space echoplanar CMRA:* With fast breath-hold or free breathing 3D EPI coronary MRA, two to four excitation pulses are followed by a short EPI read-out train [70, 71]. This takes advantage of the EPI speed while keeping the echo and acquisition time short to minimize blood flow and motion related artifacts.

*Bypass grafts:* Early CMR studies for bypass graft assessment used non-respiratory compensated, ECG-triggered 2D spin echo and gradient echo techniques. Current approaches (often used in

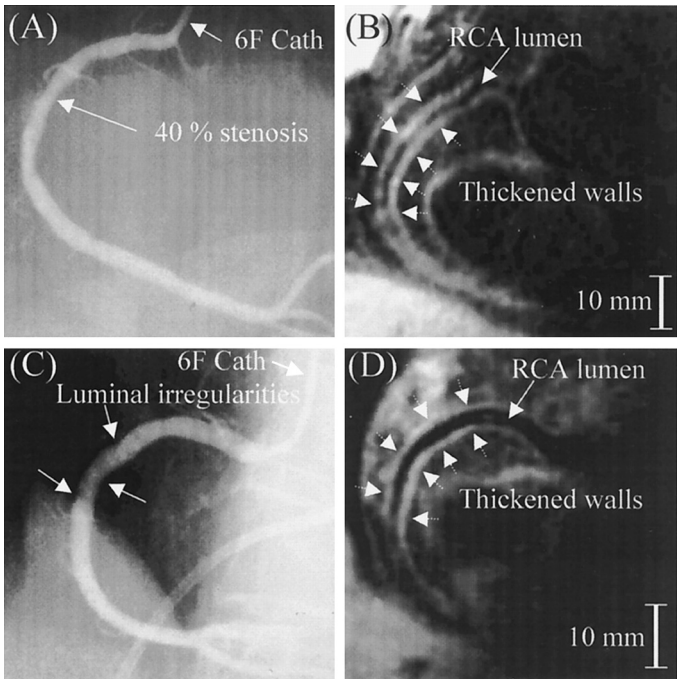


**Fig. 2.21** Black-blood 3D CMR vessel wall scans (B, D) demonstrate an irregularly thickened RCA wall (>2 mm) indicative of an increased atherosclerotic plaque burden. The inner and outer RCA walls are indicated by the white dotted arrows. Comparison is made with the corresponding diagnostic x-ray angiographic images (A, C). (Figure reproduced from: Reference 67, Kim WY, Stuber M, Börnet P. Three-dimensional black-blood cardiac magnetic resonance coronary vessel wall imaging detects positive arterial remodelling in patients with non-significant coronary artery disease. (*Circulation* 2002; **106**: 296. Reproduced with permission of the publishers.)

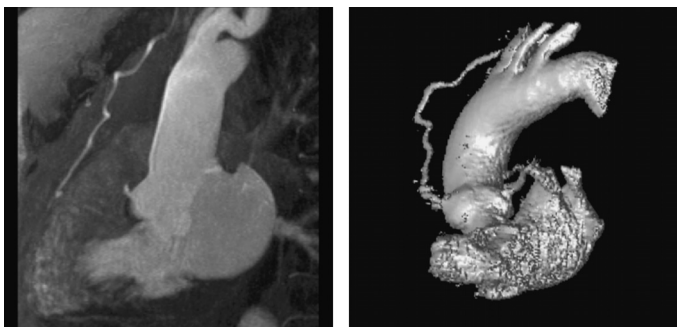

(a) (b)

**Fig. 2.22** Contrast enhanced MR angiogram of a patent LIMA graft six months post surgery. Acquisition of a 3D data set allows postprocessing with multiplanar reformation and maximum intensity projection (a). Surface rendered image is shown (b). (Images courtesy of Drs. O. Mohrs and T. Voigtlaender, Frankfurt/Main, Germany.)

combination) can be broadly divided into techniques that assess patency, such as turbo spin echo (e.g. HASTE) and MR angiography, and those that assess graft flow reserve, which can give information about graft stenosis. 3D MR angiography using rapid contrast injection (after initially performing a timing sequence to determine the onset of peak gadolinium-DTPA enhancement) is the preferred technique for assessing graft patency. Acquisition of a 3D data set allows postprocessing with multiplanar reformation and maximum intensity projection to identify grafts. Surface rendering of this 3D data set is also possible (see Fig. 2.22).

Despite recent advances in technique development, MR coronary angiography at 1.5 T produces (at best) in-plane resolution of around 0.7 mm, which is inferior to that obtained with invasive x-ray coronary angiography (around 0.3 mm). As such, currently, it cannot replace the latter for routine clinical use.

## Atherosclerosis imaging

High-resolution magnetic resonance (MR) has emerged as the leading *in vivo* imaging modality for atherosclerotic plaque characterization, given the inherent advantages of non-invasiveness and high

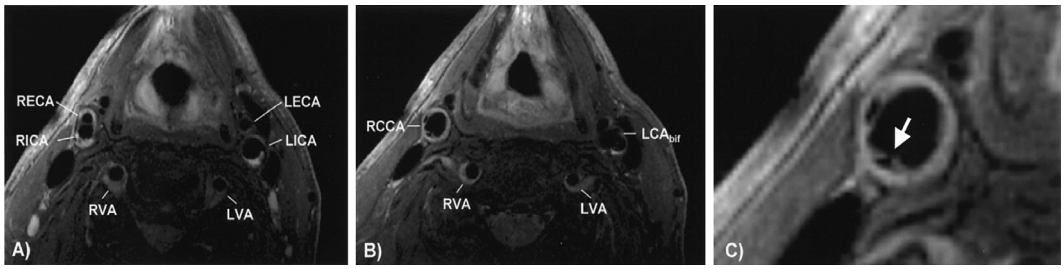


**Fig. 2.23** Example of *in vivo* carotid plaque imaging in a 61-year-old smoker who presented with recent anterior circulation transient ischemic attack (TIA). (A) Magnetic resonance $T_2$-weighted turbo-spin-echo images in a transverse plane, showing increased wall thickness of the carotid and vertebral arteries. (B) Significantly thickened vessel wall in the left carotid bifurcation (LCA). Also shown are two arteriosclerotic lesions in the right common carotid artery (RCCA) with dark lipid core and thin fibrous cap (C). Close up of right common carotid artery suggestive of plaque rupture (arrow). (Figure reproduced from: Reference 77, Wiesmann F, Robson MD, Francis JM *et al.* Visualization of the ruptured plaque by magnetic resonance imaging. *Circulation* 2003; **108**: 2542. Reproduced with permission of the publishers.)

spatial resolution. MR differentiates plaque components on the basis of biophysical and biochemical parameters such as chemical composition and concentration, water content, physical state, molecular motion, or diffusion.

Since detected MR signals rely on the relaxation times $T_1$ and $T_2$ and on proton density, the MR images can be "weighted" to the $T_1$, $T_2$, or proton density values through adaptation of the imaging parameters (such as repetition time and echo time). For example, in a $T_1$-weighted ($T_{1w}$) image, tissues with lower $T_1$ values will produce pixels with high signal intensity. Conversely, tissues with a longer $T_2$ relaxation time will appear hyperintense in a $T_2$-weighted ($T_{2w}$) image. In a proton density-weighted ($PD_W$) image the contrast relies mainly on the differences in density of water and fat protons within the tissue. This contrast is also referred to as intermediate-weighted, as it represents a combination of $T_1$ and $T_2$ contrast. Applying these different "weightings", one can produce maps with varying contrast of the same object [72]. This makes the MR method uniquely suitable for the assessment of the vascular wall [73]. Improvements in MR technology, including the development of high-sensitivity coils and faster imaging protocols, have allowed the study of atherosclerotic plaques using multicontrast ($T_{1w}$, $T_{2w}$, and $PD_w$) MR imaging [74]. MR imaging has been used for the study of atherosclerotic plaque in the human aorta [75], carotid arteries (Fig. 2.23) [76, 77], and in peripheral arteries [78]. Successful MR imaging of the coronary artery wall has been performed (Fig. 2.24) [80], but is technically demanding because of the small size and highly tortuous course of the coronaries. Additionally, to obtain artifact-free images, cardiac and respiratory motion must be reliably suppressed. Use of navigator echoes accounts for any cardiac or diaphragmatic motion and allows visualization of the coronary wall in a time-efficient way without the need for breath-holding [81].

### Studies on human atherosclerosis

*Carotid artery: In vivo* images of advanced lesions in carotid arteries were initially performed in patients referred for endarterectomy [82]. As the carotid arteries are superficial and less mobile than the aorta and the coronary arteries they pose less of a technical challenge for imaging. Some of the MR studies of carotid arterial plaques include the imaging and characterization of normal and pathological arterial walls, the quantification of plaque size, and the detection of fibrous cap "integrity". Typically the images are acquired with resolution of $0.4 \times 0.4 \times 3$ mm$^3$ using a carotid phased-array coil. Most of the *in vivo* MR plaque imaging and characterization have been performed using a multicontrast approach with high-resolution black-blood spin echo- and fast spin echo-based MR sequences. The signal from the blood flow is rendered black by the use of preparatory pulses (e.g. radiofrequency spatial saturation or inversion recovery pulses) to better visualize the adjacent vessel wall.

MR angiography (MRA) and high-resolution black-blood imaging of the vessel wall can be combined. MRA demonstrates the severity of stenotic

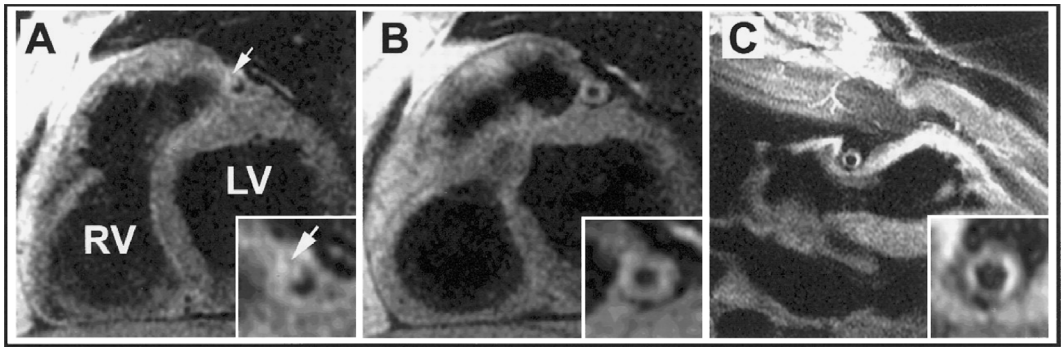


**Fig. 2.24** Human *in vivo* MR black-blood cross-sectional images that demonstrate a plaque with (presumed) deposition of fat (arrow, A) and a concentric fibrotic lesion (B) in the left anterior descending artery, and an ectatic, but atherosclerotic, right coronary artery (C). (Figure reproduced from: Reference 79, Fayad Z, Fuster V, Nikolaou K *et al.* Computed tomography and magnetic resonance imaging for non-invasive coronary angiography and plaque imaging: Current and potential future concepts. *Circulation* 2002; **106**: 2026. Reproduced with permission of the publishers.)

lesions and their spatial distribution, whereas the high-resolution black-blood wall characterization technique may show the composition of the plaques and may facilitate the risk stratification and selection of the treatment modality. Improvements in spatial resolution (<250 μm) have been possible with the design of new phased-array coils tailored for carotid imaging [83] and new imaging sequences such as long echo train fast spin echo imaging with "velocity-selective" flow suppression or double-inversion recovery preparatory pulses (black-blood imaging).

*Aorta: In vivo* black-blood MR atherosclerotic plaque characterization of the human aorta has been reported recently. Fayad *et al.* [75] assessed thoracic aorta plaque composition and size using $T_{1W}$, $T_{2W}$, and $PD_W$ images. The acquired images had a resolution of $0.8 \times 0.8 \times 5$ mm$^3$ using a torso phased-array coil. Rapid high-resolution imaging was performed with a fast spin echo sequence in conjunction with velocity-selective flow suppression preparatory pulses. Matched cross-sectional aortic imaging with MR and TEE showed a strong correlation for plaque composition and mean maximum plaque thickness.

## Cardiac magnetic resonance spectroscopy

Cardiac MRI uses the $^1$H nucleus in water and fat molecules as its only signal source. In contrast, cardiac MR spectroscopy (MRS) allows the study of many additional nuclei with a net nuclear spin, i.e. with an uneven number of protons, neutrons or both. Importantly, MRS is the only available method for the non-invasive study of cardiac metabolism without external radioactive tracers (as used, for example in positron emission tomography). Table 2.1 lists the nuclei most frequently used in cardiac MRS: $^1$H (protons from metabolites other than water and fat), $^{13}$C, $^{23}$Na and $^{31}$P. Cardiac MRS is a fascinating method but has one major limitation: Low spatial and temporal resolution. The nuclei studied with MRS have a much lower MR sensitivity than $^1$H and are present in much lower concentrations than those of $^1$H nuclei of water and fat (Table 2.1). Therefore, the resolution of MRS is several orders of magnitude lower than that of MRI.

### Basic principles of MR spectroscopy

The most extensively studied nucleus in cardiac MRS is phosphorus ($^{31}$P), and the basic principles of MRS, relevant for all nuclei, are best derived from a $^{31}$P-MRS study of the most widely used animal model, the isolated buffer-perfused rodent heart [84]. MRS is performed using an MR spectrometer, which consists of a high-field (up to 18 Tesla) superconducting magnet with a bore size ranging between ~5 cm and ~1 m. The magnet bore holds the nucleus-specific probe head with the radiofrequency (RF) coils, which are used for MR excitation and signal reception. The magnet is inter-

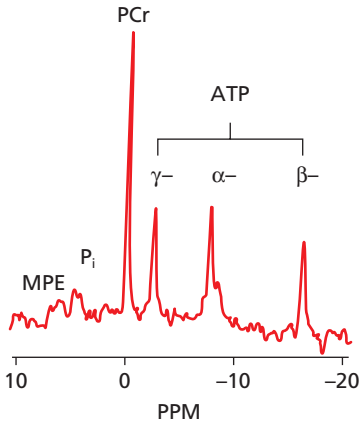


**Fig. 2.25** $^{31}$P-MR spectrum of an isolated, buffer-perfused rat heart obtained within 5 min at 7 Tesla.

faced with a control computer, a magnetic field gradient system, and an RF transmitter and receiver. The magnetic field requires homogenization with shim gradients, as MRS demands high magnetic field homogeneity. A radiofrequency impulse is sent into the RF coils for spin excitation. The resulting MR signal, the free induction decay (FID) is then recorded. The FID is subjected to Fourier transformation, which results in an MR spectrum.

A typical $^{31}$P-MR spectrum from an isolated, beating rat heart, obtained in 5 min at 7 T is shown in Fig. 2.25. A $^{31}$P-spectrum shows six resonances, corresponding to the three $^{31}$P-atoms of Adenosine Tri-phosphate (ATP), phosphocreatine (PCr), inorganic phosphate (Pi) and monophosphate esters (MPE). Different metabolites resonate at distinct frequencies, and this is termed the chemical shift phenomenon (quantified relative to the $B_0$ field in ppm = parts per million): Different positions in the molecule lead to subtle differences in the local magnetic field strength, spreading the resonance frequencies of $^{31}$P metabolites over a range of ~30 ppm. From the fully relaxed state, the area under each $^{31}$P-resonance is proportional to the amount of each $^{31}$P-nucleus in the sample, and metabolite resonances are quantified by measuring peak areas. Relative metabolite levels are calculated directly (such as the phosphocreatine/ATP ratio), and absolute metabolite concentrations are calculated by comparing tissue resonance areas to those of an external $^{31}$P-reference standard (e.g. phenylphosphonate) [85–87]. $^{31}$P-MRS has been used extensively to study the relationships between cardiac function and energy metabolism in acute ischemia/reperfusion and in chronic heart failure models [84, 88–90]. These experimental studies suggest a crucial role of altered cardiac energetics in injured myocardium.

Because of the low sensitivity of MRS, many FIDs have to be signal averaged to obtain MR spectra with a sufficient signal-to-noise ratio. Typically, for a perfused rat heart experiment at 7–12 Tesla, 100–200 FIDs are acquired and signal averaged. In MRS, it is important to account for the effects of partial saturation when selecting pulse angles and TR: A full MR signal from a given nucleus can only be obtained when the nucleus is excited from a fully relaxed spin state, i.e. when a time of at least $5 \times T_1$ has passed since the previous excitation (for example, $T_1$ of phosphocreatine at 1.5 Tesla ~4.4 s requiring TR of 22 s); "fully relaxed" spectra can therefore only be obtained with long TRs, leading to prohibitively long acquisition times. In practice, shorter TRs are used, but these yield spectra where a part of the signal is lost due to saturation effects ("partially saturated"). Since the $T_1$s of $^{31}$P-metabolites such as phosphocreatine and ATP are different ($T_1$ of phosphocreatine is ~ twice as long as $T_1$ of ATP), the extent of saturation also varies for different $^{31}$P-resonances. Thus, when quantifying partially saturated spectra, "saturation factors" need to be used for correction. These factors are determined for each metabolite by comparing fully relaxed and saturated spectra.

$^1$H has the highest MR sensitivity of all MR-detectable nuclei and very high natural abundance (Table 2.1). Many metabolites can be detected by $^1$H-MRS, such as creatine, lactate, carnitine, taurine and -$CH_3$ and -$CH_2$ resonances of lipids [91–93]. Particularly promising is the non-invasive measurement of total creatine [94, 95]. Furthermore, tissue oxygenation can be followed non-invasively by $^1$H-MRS using the oxymyoglobin and deoxymyoglobin resonances [96]. However, $^1$H-MRS is technically demanding, as we need to suppress the strong $^1$H signal from water which is 1,000,000 times more intense than the metabolite signals. Furthermore, the complex $^1$H spectra show overlapping resonances, many of which remain to be characterized. Cardiac $^1$H-MRS is only in its infancy, but the technique has enormous potential for clinical application.

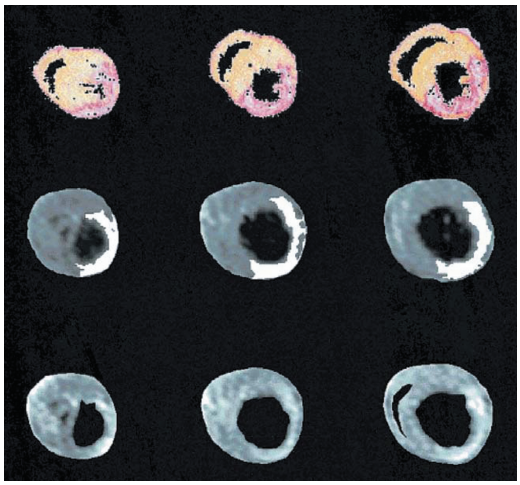

**Fig. 2.26** Bottom row: Three adjacent slices of a 3D $^{23}$Na-MRI dataset in an isolated rat heart four weeks post-MI after segmentation. Middle row: The region with signal elevation of double standard deviation over mean in the $^{23}$Na image is delineated in white, and is chosen for infarct size measurement. Top row: Corresponding histological slices with stained infarcted area. The area of increased $^{23}$Na signal intensity closely matches the histologic scar area ($r = 0.91$; $p < 0.0001$) (Figure reproduced from: Reference 88, Horn M, Weidensteiner C, Scheffer H *et al*. *Magn Reson Med* 2001; **45**: 756–764. Reproduced with permission from Wiley & Sons, New York.)

The $^{13}$C nucleus has a low natural abundance (~1%), and for a $^{13}$C-MRS experiment, the heart has to be loaded with $^{13}$C-labeled compounds such as, e.g. 1-$^{13}$C-glucose. Typically, these are added to perfusion media or infused into a coronary artery during a defined study protocol. Substrate utilization by the heart [97, 98] may then be investigated, or the activities of key enzymes or entire metabolic pathways can be quantified, e.g. citric acid cycle flux, pyruvate dehydrogenase flux and beta-oxidation of fatty acids [99–101]. Clinical applications have yet to be reported for the heart, because MR sensitivity and concentrations of $^{13}$C nuclei are too low for spatially resolved detection in human heart within an acceptable acquisition time.

$^{23}$Na-MRS is the only non-invasive method for evaluation of changes in intra and extracellular $^{23}$Na during cardiac injury [102]. Maintenance of the sarcolemmal $^{23}$Na concentration gradient (extracellular/intracellular concentration gradient ~14:1) is a requirement for normal cardiac function. A cardiac $^{23}$Na spectrum yields a single peak representing all $^{23}$Na in the heart (the total $Na^+$ signal), and for discrimination of intra and extracellular $^{23}$Na pools paramagnetic shift reagents, e.g. $[TmDOTP]^{5-}$, have to be added to the perfusate. These high molecular weight chelate complexes are distributed in the extracellular space only, and $^{23}$Na in the close vicinity of shift reagents undergoes a downfield chemical shift of its resonance frequency, so that extracellular and intracellular $^{23}$Na peaks can be discriminated. This method is being used experimentally to examine the mechanisms of intracellular $Na^+$ accumulation in ischemia-reperfusion injury [103]. Unfortunately, $^{23}$Na-MR shift reagents for clinical use are currently not yet available, so that only imaging of the total Na signal is feasible, as first demonstrated by DeLayre *et al.* [104]. However, even the total $^{23}$Na signal holds biologically important information: In acute ischemia, the total myocardial $^{23}$Na MRI signal increases because of breakdown of ion homeostasis and intra and extracellular edema formation [105]. Furthermore, the total Na signal remains significantly elevated during chronic scar formation, as we have demonstrated in an experimental model [106], because of the expansion of the extracellular space in scar (Fig. 2.26). In contrast, $^{23}$Na content is not elevated in akinetic, but stunned or hibernating myocardium [88]. For these reasons, $^{23}$Na MRI may allow detection of myocardial viability based on intrinsic tissue contrast.

## Clinical cardiac MRS methods

Almost all human cardiac MRS studies have so far been confined to the $^{31}$P nucleus. Clinical cardiac spectroscopy is a complex technique. There are hardware requirements that usually do not come with a standard CMR system: The RF generator has to be able to produce frequencies other than $^{1}$H ("broadband capability"), and a specific $^{31}$P-cardiac surface coil is needed, typically with a loop diameter of 10–15 cm. The low resolution of MRS cannot simply be offset by increasing imaging time, which, for practical reasons, is limited to 60–90 min. ECG gating is required, but, given the large voxel sizes and the already extended acquisition time, respiration gating is currently not employed. Field strength of clinical MRS systems is much lower than that of experimental systems, i.e. typically 1.5 Tesla, although 3 Tesla systems have recently become

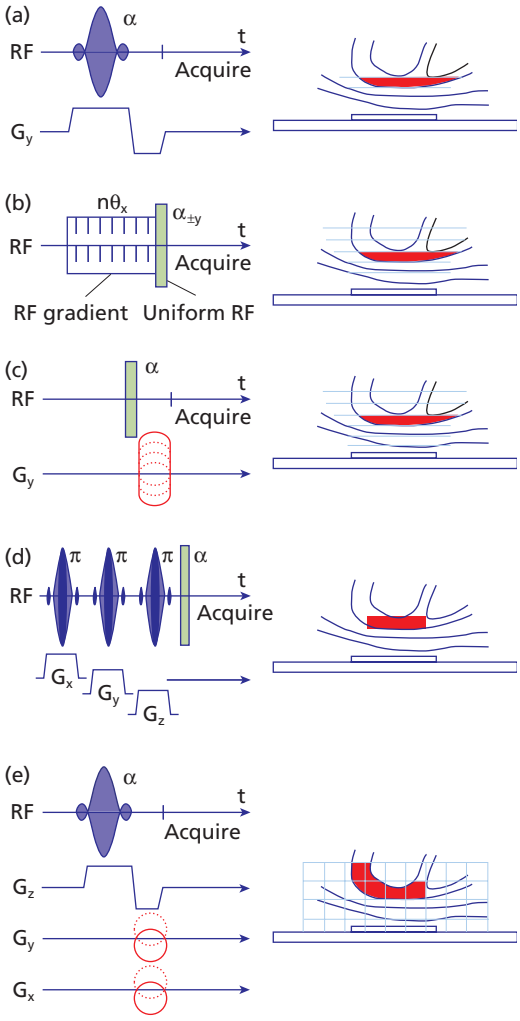


**Fig. 2.27** Basic pulse sequences for localized cardiac spectroscopy with surface coils. (a) "depth-resolved surface coil spectroscopy". A single section parallel to the plane of the surface coil is selected by applying an MR imaging gradient G in the presence of a modulated radiofrequency excitation pulse of flip angle. (b) The "rotating frame" MR method uses the gradient inherent in a surface coil to simultaneously spatially encode spectra from multiple sections parallel to the surface coil by means of application of a flip angle pulse, which is stepped in subsequent applications of the sequence. (c) The "one-dimensional chemical shift imaging" method similarly encodes multiple sections but uses an MR imaging gradient whose amplitude is stepped. (d) The "image-selected *in vivo* spectroscopy" method localizes to a single volume with selective inversion pulses applied with $G_x$, $G_y$ and $G_z$ MR imaging gradients. All eight combinations of the three pulses must be applied and the resultant signals added and subtracted. (e) A section-selective "three-dimensional chemical shift imaging" sequence employs MR imaging section selection in one dimension and phase encoding in two dimensions. (Figure reproduced from: Reference 107, Bottomley PA. MR spectroscopy of the human heart: The status and the challenges. *Radiology* 1994; **191**; 593–612. Reproduced with permission from the Radiological Society of North America.)

available. The cardiac muscle lies behind the chest wall skeletal muscle, whose $^{31}$P-signal requires suppression by means of spectroscopic localization techniques. Localization methods used for cardiac MRS include DRESS (depth-resolved surface coil spectroscopy); rotating frame; 1D-CSI (chemical shift imaging); ISIS (image-selected *in vivo* spectroscopy), and 3D-CSI. Some details are given in Fig. 2.27; for a full description of localization methods see the review by Bottomley [107]. Although less comfortable for the patient, it is currently recommended that MRS studies be performed in prone position rather than supine, as this reduces motion artifacts and brings the heart closer to the surface coil, thus improving sensitivity. $^{1}$H scout images are first obtained to select the spectroscopic voxel(s), followed by $^{31}$P-acquisition for 20–50 min. Given the low sensitivity, $^{31}$P-MRS voxel sizes have been large, typically ~30 ml. A typical $^{31}$P-MR spectrum of a healthy volunteer is shown in Fig. 2.28. Compared to the rat heart spectrum, two additional resonances are seen: 2,3-diphosphoglycerate (2,3-DPG), arising from the presence of blood (erythrocytes) in the voxel, and phosphodiesters (PDE), a signal due to membrane as well as serum phospholipids. The 2,3-diphosphoglycerate resonances overlap with the inorganic phosphate peak, which therefore cannot be detected in most human $^{31}$P-MR spectra. For relative quantification of human $^{31}$P-spectra, the phosphocreatine/ATP and phosphodiester/ATP peak area ratios are calculated. The phosphocreatine/ATP ratio is a powerful indicator of the energetic state of the heart. The meaning of the phosphodiester/ATP ratio remains poorly understood, and this ratio may not change with cardiac disease. Human $^{31}$P-resonances require correction for the effects of partial saturation according to the principles described for experimental MRS. In addition, to account for saturation, either adiabatic pulses (creating identical flip angles across the entire sample volume) or $B_1$ field characterization (taking into account variations in flip angle) are

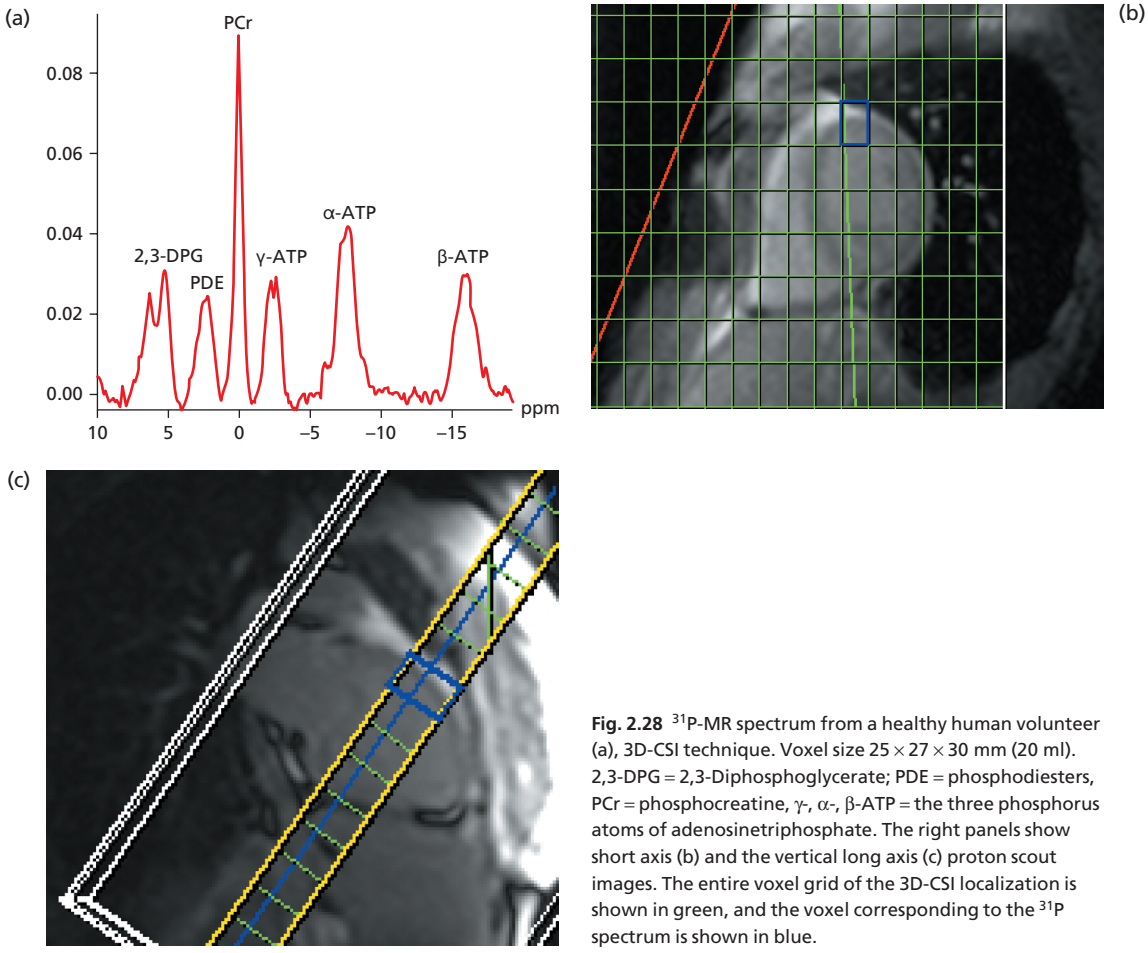


**Fig. 2.28** $^{31}$P-MR spectrum from a healthy human volunteer (a), 3D-CSI technique. Voxel size 25 × 27 × 30 mm (20 ml). 2,3-DPG = 2,3-Diphosphoglycerate; PDE = phosphodiesters, PCr = phosphocreatine, γ-, α-, β-ATP = the three phosphorus atoms of adenosinetriphosphate. The right panels show short axis (b) and the vertical long axis (c) proton scout images. The entire voxel grid of the 3D-CSI localization is shown in green, and the voxel corresponding to the $^{31}$P spectrum is shown in blue.

required. $^{31}$P-spectra should also be corrected for blood contamination: Blood contributes signal to the ATP-, 2,3-diphosphoglycerate- and phosphodiester-resonances of a cardiac $^{31}$P-spectrum. As human blood spectra show an ATP/2,3-diphosphoglycerate area ratio of ~0.11 and a phosphodiester/2,3-diphosphoglycerate area ratio of ~0.19, for blood correction, the ATP resonance area of cardiac spectra is reduced by 11% of the 2,3-diphosphoglycerate resonance area, and the phosphodiester resonance area is reduced by 19% of the 2,3-diphosphoglycerate resonance area [106].

Absolute quantification of phosphocreatine and ATP is difficult, but is an essential step for further development of clinical cardiac MRS, as the phosphocreatine/ATP ratio cannot detect simultaneous decreases of phosphocreatine and ATP, which have been demonstrated, for example, in the failing [108] or in the infarcted non-viable, myocardium [109]. Quantification of absolute $^{31}$P-metabolite levels is possible by obtaining simultaneous signal from a $^{31}$P-standard and estimates of myocardial mass based on MR imaging [110]. An alternative strategy [111] is to use simultaneous acquisition of a $^{1}$H-spectrum and to calibrate the $^{31}$P-signal to the tissue water proton content. Probably the most advanced technique in this respect is SLOOP (spectral localisation with optimum pointspread function), which allows interrogation of curved regions of interest matching the shape of the heart, and absolute quantification with high accuracy [112]. SLOOP requires a $^{31}$P reference standard, flip angle calibration, $B_1$ field mapping, and measurement of myocardial mass.

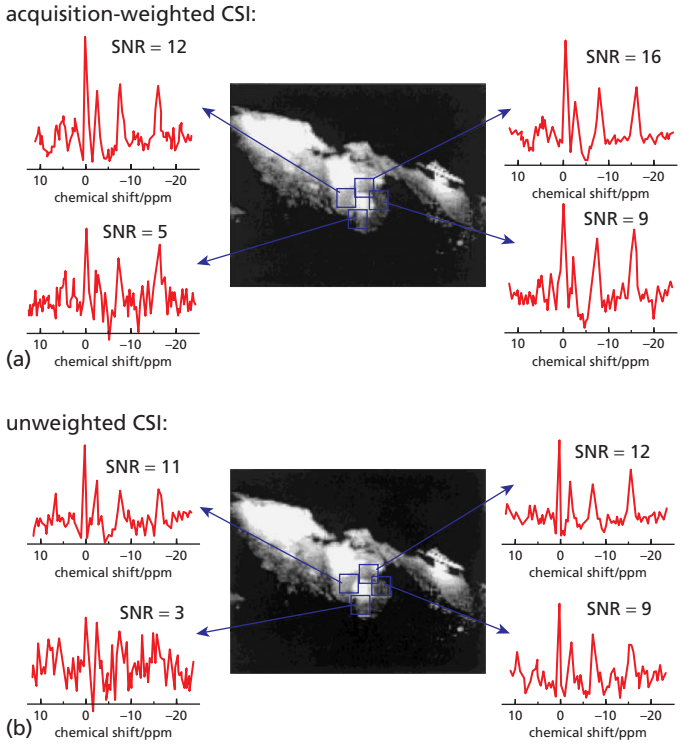


**Fig. 2.29** Results of (a) acquisition-weighted and (b) unweighted $^{31}$P-chemical shift imaging (CSI) experiment on a healthy volunteer. For both experiments, four spectra from the same voxel positions are shown. Nominal voxel size was $2.5 \times 2.5 \times 4.0$ cm$^3$, and each experiment consisted of 2048 scans synchronized to the heart beat. SNR = signal-to-noise. The spectra obtained with acquisition weighting show a considerably higher phosphocreatine/ATP ratio and a higher SNR for the phosphocreatine and ATP signals. Also, high resolution spectra from the posterior wall can be obtained. (Figure re-drawn from: Reference 113, Pohmann R, von Kienlin M. Accurate phosphorous metabolite images of the human heart by 3D acquisition-weighted CSI. *Magn Reson Med* 2001; **45**: 817–826. Re-drawn with permission from Wiley & Sons, New York.)

It has previously been impossible to interrogate the posterior wall of the human heart, because of its distance from the $^{31}$P-surface coil. Pohmann and von Kienlin [113] have recently implemented acquisition-weighted $^{31}$P-chemical shift imaging, which reduces the signal contamination between adjacent voxels, and, for the first time, $^{31}$P-spectra from the posterior wall could be obtained. Acquisition-weighting should thus be implemented for all cardiac MRS protocols (Fig. 2.29). Clinical applications of $^{31}$P-MRS are described in Chapter 7.

## Methods for clinical $^{23}$Na-MRI

Although methods for clinical $^{23}$Na-MRI are considered in this spectroscopy section, $^{23}$Na acquisition is strictly speaking an imaging technique, as there is a single frequency. Human sodium imaging requires specialist-built RF coils. Images are gated to the end-diastolic phase of the cardiac cycle but are acquired without respiratory gating due to the long duration of the scans (see Fig. 2.30). The sodium nucleus is a spin-3/2 system, which in practical terms means that the decay is bi-exponential, giving rise to two $T_2$ values. To completely characterize the signal, both components need to be obtained, and as the short $T_2$ is around 1 ms, specialist acquisition approaches are required for this. A number of such approaches have been developed [114, 115]. One benefit arising from the properties of the sodium nucleus is that $T_1$ is very short and hence it is possible to use short repetition times, so that a large number of signal averages can be acquired to improve the SNR. The high concentration of sodium in the blood pool seriously hampers detection of endocardial infarction using present methods. Developments such as advanced coil designs, higher field strengths and the use of navigated acquisitions should improve the quality of human cardiac sodium imaging.

## Perspective on MRS

Human cardiac MRS is feasible, but it is clear that a major technical development effort is still required to allow MRS to enter clinical practice. Major advances should be achievable in coil and sequence design, and through implementation of MRS at

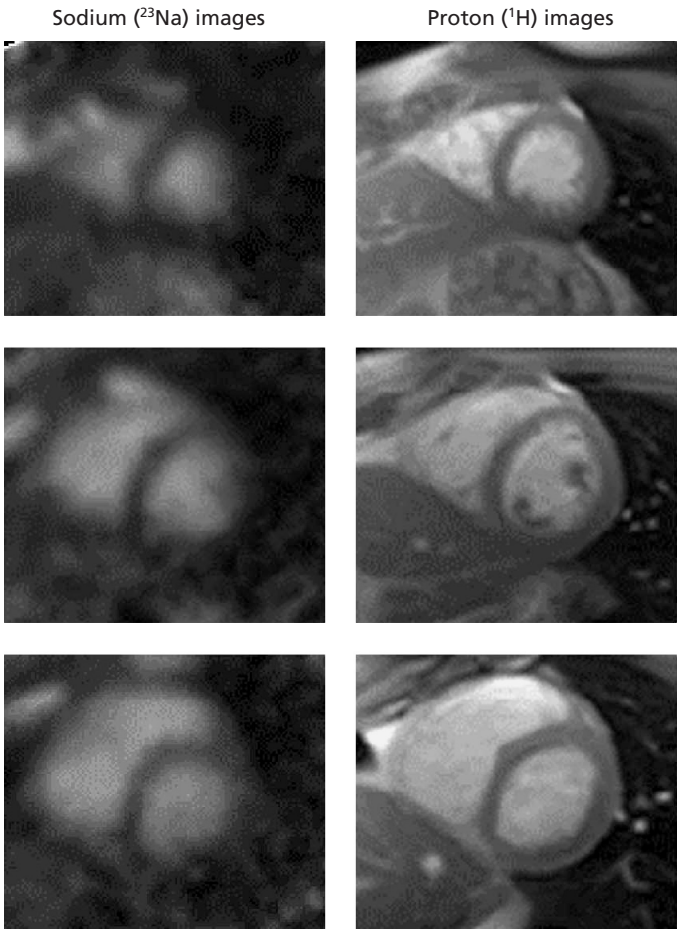


**Fig. 2.30** Here three slices from a 3D sodium data set show the concentration of the long $T_2$ in the tissue. Proton slices acquired during the same imaging session are shown for comparison. Sodium acquisition was cardiac gated and required a 22 min acquisition using our ultra-short TE CSI approach. The image quality shown here is typical for all the acquisition methods at 1.5 T.

higher field strength [116]. Standardization of cardiac MRS approaches used at different centers is also an important issue. Until that time, MRS will remain a fascinating clinical research tool, allowing insight into cardiac metabolism in various forms of human heart disease.

## Safety and contraindications

As an MR system consists of a large, static magnetic field in which RF energy is periodically released during imaging, possible hazards are associated with its use. In general, the potential hazard of implants or devices is dependent on such factors as their degree of ferromagnetism, geometry, location in the body, as well as the gradient and field strength of the imaging magnet.

In assessing whether a particular patient should be subjected to a CMR scan, the main rule, as with other investigations in medicine, is to determine the risk-benefit ratio to the patient of the proposed study. It is absolutely essential to carefully interview a patient prior to an MRI examination, and most centers would require a safety questionnaire to be completed. Whenever there is a concern about the safety of a patient with an implant, the CMR examination should be deferred until the device and the issues associated with it are clarified. Reference texts [117] and web based information (www.MRIsafety.com) on the safety of specific devices are available.

Older cerebral aneurysm clips are ferromagnetic and there are a number of reports of fatal cerebral hemorrhage after MR examinations in this

setting. Although modern aneurysm clips are non-ferromagnetic, the type of clip should be established with certainty prior to performing the examination. Previous history of eye injury with metallic shards should also be sought and an x-ray performed of the orbit if there is doubt that the metallic fragment has not been removed. Electronic devices such as cochlear implants, nerve stimulation units and a number of modern implants can be damaged or malfunction as a result of being in a magnetic field and are best avoided. Sternal wires and vascular clips are not contraindicated, although they do produce artifacts.

*Pacemakers and cardioverter defibrillators (ICDs):* Despite early reports [118] and a recent large study [119] of non-pacemaker dependent patients being safely scanned in a high field system, a pacemaker-dependent patient is generally considered as an absolute contraindication to CMR scanning. Cardiac pacemakers and ICDs present potential problems for patients undergoing MR procedures from several mechanisms including: (1) movement of the device (e.g. the pulse generator and/or leads) because of the magnetic field of the MR system; (2) MR-related heating of leads by the time-varying magnetic fields; (3) inhibition or modification of the function of the device by the electromagnetic fields used for MR procedures, and (4) inappropriate or rapid pacing due to the pulsed gradient magnetic fields and/or pulsed radiofrequency (RF) fields (i.e. electromagnetic interference with the lead acting as an antenna) [120–122]. These problems may result in serious injuries or lethal consequences for patients, as well as device malfunctions or damage [122].

*Stents:* Every year approximately 457,000 metallic coronary artery stents are placed in the US alone [123]. In patients with coronary stents, MRI is believed to be safe once endothelialization [124] has occurred, presumably because this opposes possible dislodgement [117]. Therefore, manufacturers of stents and professional associations of cardiologists [123] have traditionally recommended postponing elective MRI examinations for four to eight weeks after stent placement. However, *in vitro* and animal studies [125–127] have shown that ferromagneticity and stent migration are absent or minimal with MRI of currently available stents. Early clinical studies on the outcome of patients who undergo MRI early after coronary stent placement also indicated that CMR at 1.5 T was safe in patients early after stent implantation [128, 129]. Recently, a retrospective review of 111 patients who underwent MRI at 1.5 T (39% head/neck, 27% spine, 9% chest) fewer than eight weeks after stent placement (and treated with aspirin and thienopyridine) showed that the risk of cardiac death, MI, or need for repeat revascularization because of associated stent thrombosis was very low [130]. Although the study did not have 30 day angiographic follow-up, the results are consistent with the 30-day cardiac event rates (0.5% to 1.9%) after coronary stent placement with contemporary anti-platelet therapy in patients not undergoing MRI [131]. These findings indicate that postponing CMR until after eight weeks following coronary stenting does not seem necessary.

*Valvular prostheses:* Heart valve prostheses are all safe for CMR. These most recent recommendations supersede earlier suggestions that pre-6000 series Starr-Edwards valves might cause problems during MR. Studies at 1.5 T to 2.35 T static magnetic fields have shown that there is no hazardous deflection during exposure of the magnetic field [117, 132].

*Claustrophobia:* Despite the development of shorter magnets, and more open designs, up to 10% of patients may experience varying degrees of claustrophobia. In our experience, the number is nearer to 5% [41], which can be reduced even further to about 2% of patients by the use of explanation, reassurance and, when necessary, light sedation [133].

## Acknowledgements

The authors thank Drs Saul Myerson and Damian Tyler for critical review of various subsections of this chapter. We are also deeply grateful to the late Dr Frank Wiesmann, who played a crucial part in atherosclerosis imaging at our unit.

## References

1. Bloch F. Nuclear induction. *Physical Review (Physics)* 1946; 460–473.
2. Purcell E, Torrey, H, Pound R. Resonance adsorption by nuclear masgnetic moments in a solid. *Physical Review (Physics)* 1946; 37–38.
3. Lauterbur P. Image formation by induced local

interactions: examples employing nuclear magnetic resonance. *Nature* 1973; **242**: 190–191.
4. Garlick PB, Radda GK, Seeley PJ. Phosphorus NMR studies on perfused heart. *Biochem Biophys Res Commun*. 1977; **74**: 1256–1262.
5. Jacobus WE, Taylor GJT, Hollis DP *et al*. Phosphorus nuclear magnetic resonance of perfused working rat hearts. *Nature* 1977; **265**: 756–758.
6. Goldsmith M, Koutcher JA, Damadian R. Nuclear magnetic resonance in cancer. Application of NMR malignancy index to human lung tumors. *Br J Cancer* 1977; **36**: 235–242.
7. Anderson LJ, Holden S, Davis B *et al*. Cardiovascular $T_2$-star ($T_2^*$) magnetic resonance for the early diagnosis of myocardial iron overload. *Eur Heart J*. 2001; **22**: 2171–2179.
8. Bryant DJ, Payne JA, Firmin DN *et al*. Measurement of flow with NMR imaging using a gradient pulse and phase difference technique. *J Comput Assist Tomogr* 1984; **8**: 588–593.
9. Chia JM, Fischer SE, Wickline SA *et al*. Performance of QRS detection for cardiac magnetic resonance imaging with a novel vectorcardiographic triggering method. *J Magn Reson Imaging* 2000; **12**: 678–688.
10. Larson AC, White RD, Laub G *et al*. Self-gated cardiac cine MRI. *Magn Reson Med* 2004; **51**: 93–102.
11. Bellenger NG, Davies LC, Francis JM *et al*. Reduction in sample size for studies of remodeling in heart failure by the use of cardiovascular magnetic resonance. *J Cardiovasc Magn Reson* 2000; **2**: 271–278.
12. Grothues F, Smith GC, Moon JC *et al*. Comparison of interstudy reproducibility of cardiovascular magnetic resonance with two-dimensional echocardiography in normal subjects and in patients with heart failure or left ventricular hypertrophy. *Am J Cardiol* 2002; **90**: 29–34.
13. Alfakih K, Plein S, Thiele H *et al*. Normal human left and right ventricular dimensions for MRI as assessed by turbo gradient echo and steady-state free precession imaging sequences. *J Magn Reson Imaging* 2003; **17**: 323–329.
14. Lorenz CH, Walker ES, Morgan VL *et al*. Normal human right and left ventricular mass, systolic function, and gender differences by cine magnetic resonance imaging. *J Cardiovasc Magn Reson* 1999; **1**: 7–21.
15. Helbing WA, Rebergen SA, Maliepaard C *et al*. Quantification of right ventricular function with magnetic resonance imaging in children with normal hearts and with congenital heart disease. *Am Heart J* 1995; **130**: 828–837.
16. Helbing WA, Bosch HG, Maliepaard C *et al*. Comparison of echocardiographic methods with magnetic resonance imaging for assessment of right ventricular function in children. *Am J Cardiol* 1995; **76**: 589–594.
17. Alfakih K, Plein S, Bloomer T *et al*. Comparison of right ventricular volume measurements between axial and short axis orientation using steady-state free precession magnetic resonance imaging. *J Magn Reson Imaging* 2003; **18**: 25–32.
18. Pennell DJ, Underwood SR, Manzara CC *et al*. Magnetic resonance imaging during dobutamine stress in coronary artery disease. *Am J Cardiol* 1992; **70**: 34–40.
19. Fayad ZA, Connick TJ, Axel L. An improved quadrature or phased-array coil for MR cardiac imaging. *Magn Reson Med* 1995; **34**: 186–193.
20. Cerqueira MD, Weissman NJ, Dilsizian VJ *et al*. Standardized myocardial segmentation and nomenclature for tomographic imaging of the heart. A statement for healthcare professionals from the Cardiac Imaging Committee of the Council on Clinical Cardiology of the American Heart Association. *Int J Cardiovasc Imaging* 2002; **18**: 539–542.
21. Nagel E, Lehmkuh HB, Bocksch W *et al*. Non-invasive diagnosis of ischemia-induced wall motion abnormalities with the use of high-dose dobutamine stress MRI: Comparison with dobutamine stress echocardiography. *Circulation* 1999; **99**: 763–770.
22. Wahl A, Roethemeyer S, Paetsch I *et al*. High Dose dobutamine stress MRI for follow-up after coronary revascularization procedures in patients with wall motion abnormalities at rest. *J Cardiovasc Magn Reson* 2002; **4**: 22–23.
23. Zerhouni EA, Parish DM, Rogers WJ *et al*. Human heart: Tagging with MR imaging—a method for noninvasive assessment of myocardial motion. *Radiology* 1988; **169**: 59–63.
24. Mosher TJ, Smith MB. A DANTE tagging sequence for the evaluation of translational sample motion. *Magn Reson Med* 1990; **15**: 334–339.
25. Axel L, Dougherty L. Heart wall motion: Improved method of spatial modulation of magnetization for MR imaging. *Radiology* 1989; **172**: 349–350.
26. Bolster BD Jr, McVeigh ER, Zerhouni EA. Myocardial tagging in polar coordinates with use of striped tags. *Radiology* 1990; **177**: 769–772.
27. Ryf S, Spiegel MA, Gerber M *et al*. Myocardial tagging with 3D-CSPAMM. *J Magn Reson Imaging* 2002; **16**: 320–325.
28. Croisille P, Guttman MA, Atalar E *et al*. Precision of myocardial contour estimation from tagged MR images with a "black-blood" technique. *Acad Radiol* 1998; **5**: 93–100.
29. Hennig J, Schneider B, Peschl S. Analysis of myocardial motion based on velocity measurements with a black-blood prepared segmented gradient-echo sequence: Methodology and applications to normal volunteers and patients. *J Magn Reson Imaging* 1998; **8**: 868–877.
30. Gilson WD, Yang Z, French BA *et al*. Measurement of myocardial mechanics in mice before and after infarction using multislice displacement-encoded MRI with

3D motion encoding. *Am J Physiol Heart Circ Physiol* 2004; **288**: H1491–1497.

31. Wesbey G, Higgins C, McNamara M *et al*. Effect of gadolinium-DTPA on the magnetic relaxation times of normal and infarcted myocardium. *Radiology* 1984; **153**: 165–169.
32. Simonetti OP, Kim RJ, Fieno DS *et al*. An improved MR imaging technique for the visualization of myocardial infarction. *Radiology* 2001; **218**: 215–223.
33. Sandstede JJ, Pabst T, Beer M *et al*. Assessment of myocardial infarction in humans with (23)Na MR imaging: Comparison with cine MR imaging and delayed contrast enhancement. *Radiology* 2001; **221**: 222–228.
34. Kim RJ, Fieno DS, Parrish TB *et al*. Relationship of MRI delayed contrast enhancement to irreversible injury, infarct age, and contractile function. *Circulation* 1999; **100**: 1992–2002.
35. Choi KM, Kim RJ, Gubernikoff G *et al*. Transmural extent of acute myocardial infarction predicts long-term improvement in contractile function. *Circulation* 2001; **104**: 1101–1107.
36. Selvanayagam JB, Kardos A, Francis JM *et al*. Value of delayed-enhancement cardiovascular magnetic resonance imaging in predicting myocardial viability after surgical revascularization. *Circulation* 2004; **110**: 1535–1541.
37. Wu E, Judd RM, Vargas JD *et al*. Visualisation of presence, location, and transmural extent of healed Q-wave and non-Q-wave myocardial infarction. *Lancet* 2001; **357**: 21–28.
38. Wagner A, Mahrholdt H, Holly TA *et al*. Contrast-enhanced MRI and routine single photon emission computed tomography (SPECT) perfusion imaging for detection of subendocardial myocardial infarcts: An imaging study. *Lancet* 2003; **361**: 374–379.
39. Wu KC, Zerhouni EA, Judd RM *et al*. Prognostic significance of microvascular obstruction by magnetic resonance imaging in patients with acute myocardial infarction. *Circulation* 1998; **97**: 765–772.
40. Wu KC, Kim RJ, Bluemke DA *et al*. Quantification and time course of microvascular obstruction by contrast-enhanced echocardiography and magnetic resonance imaging following acute myocardial infarction and reperfusion. *J Am Coll Cardiol* 1998; **32**: 1756–1764.
41. Selvanayagam JB, Petersen SE, Francis JM *et al*. Effects of off-pump versus on-pump coronary surgery on reversible and irreversible myocardial injury: A randomized trial using cardiovascular magnetic resonance imaging and biochemical markers. *Circulation* 2004; **109**: 345–350.
42. Selvanayagam JB, Porto I, Channon K *et al*. Troponin elevation following percutaneous coronary intervention directly represents the extent of irreversible myocardial injury: Insights from cardiovascular magnetic resonance imaging. *Circulation* 2005; **111**: 1027–1032.
43. Kim RJ, Wu E, Rafael A. The use of contrast-enhanced magnetic resonance imaging to identify reversible myocardial dysfunction. *N Engl J Med* 2000; **343**: 1445–1453.
44. Ricciardi MJ, Wu E, Davidson CJ *et al*. Visualization of discrete microinfarction after percutaneous coronary intervention associated with mild creatine kinase-MB elevation. *Circulation* 2001; **103**: 2780–2783.
45. Wilke N, Jerosch-Herold M, Stillman AE *et al*. Concepts of myocardial perfusion imaging in magnetic resonance imaging. *Magn Reson Q*. 1994; **10**: 249–286.
46. Jerosch-Herold M, Wilke N, Stillman AE. Magnetic resonance quantification of the myocardial perfusion reserve with a Fermi function model for constrained deconvolution. *Med Phys* 1998; **25**: 73–84.
47. Nagel E, Klein C, Paetsch I *et al*. Magnetic resonance perfusion measurements for the non-invasive detection of coronary artery disease. *Circulation* 2003; **108**: 432–437.
48. Cerqueira MD, Verani MS, Schwaiger M *et al*. Safety profile of adenosine stress perfusion imaging: Results from the Adenoscan Multicenter Trial Registry. *J Am Coll Cardiol* 1994; **23**: 384–389.
49. Al-Saadi N, Nagel E, Gross M *et al*. Non-invasive detection of myocardial ischemia from perfusion reserve based on cardiovascular magnetic resonance. *Circulation* 2000; **101**: 1379–1383.
50. Jerosch-Herold M, Wilke N. MR first pass imaging: Quantitative assessment of transmural perfusion and collateral flow. *Int J Card Imaging* 1997; **13**: 205–218.
51. Wilke N, Simm C, Zhang J *et al*. Contrast-enhanced first pass myocardial perfusion imaging: Correlation between myocardial blood flow in dogs at rest and during hyperemia. *Magn Reson Med* 1993; **29**: 485–497.
52. Larsson HB, Fritz-Hansen T, Rostrup E *et al*. Myocardial perfusion modeling using MRI. *Magn Reson Med* 1996; **35**: 716–726.
53. Jerosch-Herold M, Seethamraju RT, Swingen CM *et al*. Analysis of myocardial perfusion MRI. *J Magn Reson Imaging* 2004; **19**: 758–770.
54. Wacker CM, Hartlep AW, Pfleger S *et al*. Susceptibility-sensitive magnetic resonance imaging detects human myocardium supplied by a stenotic coronary artery without a contrast agent. *J Am Coll Cardiol* 2003; **41**: 834–840.
55. Wacker CM, Bock M, Hartlep AW *et al*. Changes in myocardial oxygenation and perfusion under pharmacological stress with dipyridamole: Assessment using $T_2^*$ and $T_1$ measurements. *Magn Reson Med* 1999; **41**: 686–695.
56. Friedrich MG, Niendorf T, Schulz-Menger J *et al*. Blood oxygen level-dependent magnetic resonance imaging

in patients with stress-induced angina. *Circulation*. 2003; **108**: 2219–2223.
57. Mostbeck GH, Caputo GR, Higgins CB. MR measurement of blood flow in the cardiovascular system. *AJR Am J Roentgenol* 1992; **159**: 453–461.
58. Rebergen SA, van der Wall EE, Doornbos J *et al*. Magnetic resonance measurement of velocity and flow: Technique, validation, and cardiovascular applications. *Am Heart J* 1993; **126**: 1439–1456.
59. Didier D, Ratib O, Friedli B *et al*. Cine gradient-echo MR imaging in the evaluation of cardiovascular diseases. *Radiographics* 1993; **13**: 561–573.
60. Suzuki J, Caputo GR, Kondo C *et al*. Cine MR imaging of valvular heart disease: Display and imaging parameters affect the size of the signal void caused by valvular regurgitation. *AJR Am J Roentgenol* 1990; **155**: 723–727.
61. Mohiaddin RH, Pennell DJ. MR blood flow measurement. Clinical application in the heart and circulation. *Cardiol Clin* 1998; **16**: 161–187.
62. Kondo C, Caputo GR, Semelka R *et al*. Right and left ventricular stroke volume measurements with velocity-encoded cine MR imaging: *In vitro* and *in vivo* validation. *AJR Am J Roentgenol* 1991; **157**: 9–16.
63. Hundley WG, Li HF, Lange RA *et al*. Assessment of left-to-right intracardiac shunting by velocity-encoded, phase-difference magnetic resonance imaging. A comparison with oximetric and indicator dilution techniques. *Circulation* 1995; **91**: 2955–2960.
64. Caputo GR, Kondo C, Masui T *et al*. Right and left lung perfusion: *In vitro* and *in vivo* validation with oblique-angle, velocity-encoded cine MR imaging. *Radiology* 1991; **180**: 693–698.
65. Li D, Paschal CB, Haacke EM *et al*. Coronary arteries: Three-dimensional MR imaging with fat saturation and magnetization transfer contrast. *Radiology* 1993; **187**: 401–406.
66. Manning WJ, Li W, Boyle NG *et al*. Fat-suppressed breath-hold magnetic resonance coronary angiography. *Circulation* 1993; **87**: 94–104.
67. Kim WY, Stuber M, Börnet P. Three-dimensional black-blood cardiac magnetic resonance coronary vessel wall imaging detects positive arterial remodelling in patients with non-significant coronary artery disease. *Circulation* 2002; **106**: 296.
68. Botnar R, Stuber M, Danias P *et al*. Coronary magnetic resonance angiography. In: Manning WJ & Pennell DJ, eds. *Cardiovascular Magnetic Resonance*. Churchill Livingstone, Philadelphia, 2001.
69. Botnar RM, Stuber M, Danias PG *et al*. Improved coronary artery definition with $T_2$-weighted, free-breathing, three-dimensional coronary MRA. *Circulation* 1999; **99**: 3139–3148.
70. Wielopolski PA, Manning WJ, Edelman RR. Single breath-hold volumetric imaging of the heart using magnetization-prepared 3-dimensional segmented echo planar imaging. *J Magn Reson Imaging* 1995; **5**: 403–409.
71. Slavin GS, Riederer SJ, Ehman RL. Two-dimensional multishot echo-planar coronary MR angiography. *Magn Reson Med* 1998; **40**: 883–889.
72. Fayad ZA, Fuster V. Clinical imaging of the high-risk or vulnerable atherosclerotic plaque. *Circ Res* 2001; **89**: 305–316.
73. Herfkens RJ, Higgins CB, Hricak H *et al*. Nuclear magnetic resonance imaging of atherosclerotic disease. *Radiology* 1983; **148**: 161–166.
74. Fayad ZA, Fuster V. Characterization of atherosclerotic plaques by magnetic resonance imaging. *Ann N Y Acad Sci* 2000; **902**: 173–186.
75. Fayad ZA, Nahar T, Fallon JT *et al*. *In vivo* magnetic resonance evaluation of atherosclerotic plaques in the human thoracic aorta: A comparison with transesophageal echocardiography. *Circulation* 2000; **101**: 2503–2509.
76. Yuan C, Beach KW, Smith LH Jr *et al*. Measurement of atherosclerotic carotid plaque size *in vivo* using high resolution magnetic resonance imaging. *Circulation* 1998; **98**: 2666–2671.
77. Wiesmann F, Robson MD, Francis JM *et al*. Visualization of the ruptured plaque by magnetic resonance imaging. *Circulation* 2003; **108**: 2542.
78. Coulden RA, Moss H, Graves MJ *et al*. High resolution magnetic resonance imaging of atherosclerosis and the response to balloon angioplasty. *Heart* 2000; **83**: 188–191.
79. Fayad Z, Fuster V, Nikolaou K *et al*. Computed tomography and magnetic resonance imaging for non-invasive coronary angiography and plaque imaging: Current and potential future concepts. *Circulation* 2002; **106**: 2026.
80. Fayad ZA, Fuster V, Fallon JT *et al*. Non-invasive *in vivo* human coronary artery lumen and wall imaging using black-blood magnetic resonance imaging. *Circulation* 2000; **102**: 506–510.
81. Botnar RM, Kim WY, Bornert P *et al*. 3D coronary vessel wall imaging utilizing a local inversion technique with spiral image acquisition. *Magn Reson Med* 2001; **46**: 848–854.
82. Toussaint JF, LaMuraglia GM, Southern JF *et al*. Magnetic resonance images of lipid, fibrous, calcified, hemorrhagic, and thrombotic components of human atherosclerosis *in vivo*. *Circulation* 1996; **94**: 932–938.
83. Hayes CE, Mathis CM, Yuan C. Surface coil phased arrays for high-resolution imaging of the carotid arteries. *J Magn Reson Imaging* 1996; **6**: 109–112.

84. Neubauer S, Ingwall JS. Verapamil attenuates ATP depletion during hypoxia: $^{31}$P NMR studies of the isolated rat heart. *J Mol Cell Card* 1989; **21**: 1163–1178.
85. Ingwall JS. Phosphorus nuclear magnetic resonance spectroscopy of cardiac and skeletal muscles. *Am J Physiol* 1982; **242**: H729–744.
86. Neubauer S, Ertl G, Krahe T *et al*. Experimental and clinical possibilities of MR spectroscopy of the heart. *Z Kardiol* 1991; **80**: 25–36, in German.
87. Clarke K, Stewart LC, Neubauer S *et al*. Extracellular volume and trans-sarcolemmal proton movement during ischemia and reperfusion: a $^{31}$P NMR spectroscopic study of the isovolumic rat heart. *NMR Biomed* 1993; **6**: 278–286.
88. Horn M, Weidensteiner C, Scheffer H *et al*. Detection of myocardial viability based on measurement of sodium content: A (23)Na-NMR study. *Magn Reson Med* 2001; **45**: 756–764.
89. Liao R, Nascimben L, Friedrich J *et al*. Decreased energy reserve in an animal model of dilated cardiomyopathy. Relationship to contractile performance. *Circ Res* 1996; **78**: 893–902.
90. Zhang J, Wilke N, Wang Y *et al*. Functional and bioenergetic consequences of postinfarction left ventricular remodeling in a new porcine model. MRI and $^{31}$P-MRS study. *Circulation* 1996; **94**: 1089–1100.
91. Ugurbil K, Petein M, Madian R *et al*. High resolution proton NMR studies of perfused rat hearts. *FEBS Lett* 1984; **167**: 73–78.
92. Balschi JA, Hetherington HP, Bradley EL Jr *et al*. Water-suppressed one-dimensional $^{1}$H NMR chemical shift imaging of the heart before and after regional ischemia. *NMR in Biomedicine* 1995; **8**: 79–86.
93. Balschi JA, Hai JO, Wolkowicz PE *et al*. $^{1}$H NMR measurement of triacylglycerol accumulation in the postischemic canine heart after transient increase of plasma lipids. *J Mol Cell Cardiol* 1997; **29**: 471–480.
94. Bottomley PA, Weiss RG. Non-invasive localized MR quantification of creatine kinase metabolites in normal and infarcted canine myocardium. *Radiology* 2001; **219**: 411–418.
95. Schneider J, Fekete E, Weisser A *et al*. Reduced (1)H-NMR visibility of creatine in isolated rat hearts. *Magn Reson Med* 2000; **43**: 497–502.
96. Kreutzer U, Mekhamer Y, Chung Y *et al*. Oxygen supply and oxidative phosphorylation limitation in rat myocardium in situ. *Am J Physiol Heart Circ Physiol* 2001; **280**: H2030–2037.
97. Solomon MA, Jeffrey FM, Storey CJ *et al*. Substrate selection early after reperfusion of ischemic regions in the working rabbit heart. *Magn Reson Med* 1996; **35**: 820–826.
98. Malloy CR, Jones JG, Jeffrey FM *et al*. Contribution of various substrates to total citric acid cycle flux and anaplerosis as determined by $^{13}$C isotopomer analysis and $O_2$ consumption in the heart. *Magma* 1996; **4**: 35–46.
99. Lewandowski ED. Cardiac carbon 13 magnetic resonance spectroscopy: On the horizon or over the rainbow? *J Nucl Cardiol* 2002; **9**: 419–428.
100. Burgess SC, Babcock EE, Jeffrey FM *et al*. NMR indirect detection of glutamate to measure citric acid cycle flux in the isolated perfused mouse heart. *FEBS Lett* 2001; **505**: 163–167.
101. Weiss RG. $^{13}$C-NMR for the study of intermediary metabolism. *Magma* 1998; **6**: 132.
102. Kohler SJ, Perry SB, Stewart LC *et al*. Analysis of $^{23}$Na NMR spectra from isolated perfused hearts. *Magn Reson Med* 1991; **18**: 15–27.
103. Clarke K, Cross HR, Keon CA *et al*. Cation MR spectroscopy ($^{7}$Li, $^{23}$Na, $^{39}$K and $^{87}$Rb). *Magma* 1998; **6**: 105–106.
104. DeLayre JL, Ingwall JS, Malloy C *et al*. Gated sodium-23 nuclear magnetic resonance images of an isolated perfused working rat heart. *Science*. 1981; **212**: 935–936.
105. Kim RJ, Lima JAC, Chen EL *et al*. Fast $^{23}$Na magnetic resonance imaging of acute reperfused myocardial infarction. Potential to assess myocardial viability. *Circulation* 1997; **95**: 1877–1885.
106. Neubauer S, Krahe T, Schindler R *et al*. $^{31}$P magnetic resonance spectroscopy in dilated cardiomyopathy and coronary artery disease. Altered cardiac high-energy phosphate metabolism in heart failure. *Circulation* 1992; **86**: 1810–1818.
107. Bottomley PA. MR spectroscopy of the human heart: The status and the challenges. *Radiology* 1994; **191**: 593–612.
108. Shen W, Asai K, Uechi M *et al*. Progressive loss of myocardial ATP due to a loss of total purines during the development of heart failure in dogs: A compensatory role for the parallel loss of creatine. *Circulation* 1999; **100**: 2113–2118.
109. Yabe T, Mitsunami K, Inubushi T *et al*. Quantitative measurements of cardiac phosphorus metabolites in coronary artery disease by $^{31}$P magnetic resonance spectroscopy. *Circulation* 1995; **92**: 15–23.
110. Bottomley PA, Hardy CJ, Roemer PB. Phosphate metabolite imaging and concentration measurements in human heart by nuclear magnetic resonance. *Magn Reson Med* 1990; **14**: 425–434.
111. Bottomley PA, Atalar E, Weiss RG. Human cardiac high-energy phosphate metabolite concentrations by 1D-resolved NMR spectroscopy. *Magn Reson Med* 1996; **35**: 664–670.

112. Meininger M, Landschutz W, Beer M. Concentrations of human cardiac phosphorus metabolites determined by SLOOP $^{31}$P NMR spectroscopy. *Magn Reson Med* 1999; **41**: 657–663.
113. Pohmann R, von Kienlin M. Accurate phosphorus metabolite images of the human heart by 3D acquisition-weighted CSI. *Magn Reson Med* 2001; **45**: 817–826.
114. Boada FE, Gillen JS, Shen GX *et al.* Fast three dimensional sodium imaging. *Magn Reson Med* 1997; **37**: 706–715.
115. Pabst T, Sandstede J, Beer M *et al.* Optimization of ECG-triggered 3D (23)Na MRI of the human heart. *Magn Reson Med* 2001; **45**: 164–166.
116. Lee RF, Giaquinto R, Constantinides C *et al.* A broadband phased-array system for direct phosphorus and sodium metabolic MRI on a clinical scanner. *Magn Reson Med* 2000; **43**: 269–277.
117. Shellock FG. *Guide to MR Procedures and Metallic Objects: Update 2001* [7th edn]. Lippincott, Williams and Wilkins Healthcare, Philadelphia, 2001.
118. Vahlhaus C, Sommer T, Lewalter T *et al.* Interference with cardiac pacemakers by magnetic resonance imaging: Are there irreversible changes at 0.5 Tesla? *Pacing Clin Electrophysiol* 2001; **24**: 489–495.
119. Martin ET, Coman JA, Owen W *et al.* Cardiac pacemakers and MRI: Safe evaluation of 47 patients using a 1.5 Tesla MR system without altering pacemaker or imaging parameters. *JACC* 2004; **43**: 1315–1324.
120. Achenbach S, Moshage W, Diem B *et al.* Effects of magnetic resonance imaging on cardiac pacemakers and electrodes. *Am Heart J* 1997; **134**: 467–473.
121. Duru F, Luechinger R, Candinas R. MR imaging in patients with cardiac pacemakers. *Radiology* 2001; **219**: 856–858.
122. Shellock FG, Tkach JA, Ruggieri PM *et al.* Cardiac pacemakers, ICDs, and loop recorder: Evaluation of translational attraction using conventional ("long-bore") and "short-bore" 1.5- and 3.0-Tesla MR systems. *J Cardiovasc Magn Reson* 2003; **5**: 387–397.
123. American Heart Association. *Heart and Stroke Statistical Update.* American Heart Association, Dallas, TX, 2002.
124. Roubin GS, Robinson KA, King SB, 3$^{rd}$ *et al.* Early and late results of intracoronary arterial stenting after coronary angioplasty in dogs. *Circulation*. 1987; **76**: 891–897.
125. Hug J, Nagel E, Bornstedt A *et al.* Coronary arterial stents: Safety and artifacts during MR imaging. *Radiology* 2000; **216**: 781–787.
126. Scott NA, Pettigrew RI. Absence of movement of coronary stents after placement in a magnetic resonance imaging field. *Am J Cardiol* 1994; **73**: 900–901.
127. Strohm O, Kivelitz D, Gross W *et al.* Safety of implantable coronary stents during $^{1}$H-magnetic resonance imaging at 1.0 and 1.5 T. *J Cardiovasc Magn Reson* 1999; **1**: 239–245.
128. Schroeder AP, Houlind K, Pedersen EM *et al.* Magnetic resonance imaging seems safe in patients with intracoronary stents. *J Cardiovasc Magn Reson* 2000; **2**: 43–49.
129. Kramer CM, Rogers WJ Jr, Pakstis DL. Absence of adverse outcomes after magnetic resonance imaging early after stent placement for acute myocardial infarction: A preliminary study. *J Cardiovasc Magn Reson* 2000; **2**: 257–261.
130. Gerber TC, Fasseas P, Lennon RJ *et al.* Clinical safety of magnetic resonance imaging early after coronary artery stent placement. *J Am Coll Cardiol* 2003; **42**: 1295–1298.
131. Orford JL, Lennon R, Melby S *et al.* Frequency and correlates of coronary stent thrombosis in the modern era: Analysis of a single center registry. *J Am Coll Cardiol* 2002; **40**: 1567–1572.
132. Soulen RL, Budinger TF, Higgins CB. Magnetic resonance imaging of prosthetic heart valves. *Radiology* 1985; **154**: 705–707.
133. Francis JM, Pennell DJ. Treatment of claustrophobia for cardiovascular magnetic resonance: Use and effectiveness of mild sedation. *J Cardiovasc Magn Reson* 2000; **2**: 139–141.